

# Application of the CBM Micro Vertex Detector for Dielectron Analysis

Dissertation zur Erlangung des Doktorgrades der  
Naturwissenschaften

vorgelegt am  
Fachbereich Physik  
der Goethe-Universität  
in Frankfurt am Main

durchgeführt am  
GSI Helmholtzzentrum für Schwerionenforschung,  
Darmstadt

Frankfurt am Main, den 31.08.2016

vom Fachbereich Physik der  
Goethe-Universität als Dissertation angenommen.

Dekan: Prof. Dr. Rene Reifarth  
Gutachter: Prof. Dr. Joachim Stroth  
Datum der Disputation:

## Abstract

The **C**ompressed **B**aryonic **M**atter (CBM) is a fixed target experiment that is going to be installed at the future accelerator FAIR (**F**acility for **A**ntiproton and **I**on **R**esearch in Darmstadt, Germany). The CBM physics programme is focused on the study of the properties of baryonic matter at high density and medium temperature. This region of the QCD phase diagram can be reached in heavy-ion collisions at energies available at FAIR. Measurement of diagnostic probes of the early and dense phase of the fireball evolution offers the possibility to find signatures of partonic degrees of freedom, and to discover the conjectured first order deconfinement phase transition and its critical endpoint. Another important goal is the study of in-medium modifications of hadron properties in order to shed light on the phenomenon of chiral symmetry restoration in dense hadronic and partonic matter [18].

Particles containing charm quarks are expected to be created in the very first stage of the reaction. The light vector mesons  $\rho$ ,  $\omega$  and  $\phi$  are continuously produced during the reaction and have a small chance to decay into a lepton pair. Low mass electron (muon) pairs are considered to be excellent probes of the processes taking place in the interior of extreme states of matter formed in the collision zone of heavy-ion collisions. Since leptons are not subject to the strong force they allow an unobstructed view into the fireball. Especially the  $\rho$  meson is a good candidate with its short life time of around  $1.3 \text{ fm}/c$  compared to expected  $10 \text{ fm}/c$  of the fireball.

However, the reconstructed distribution of electron pairs contains in addition contributions from mesons decaying after freeze-out and from combinatorial pairs. Single electron or positron tracks from incompletely detected  $\gamma$ -conversions and Dalitz decays of  $\pi^0$ -mesons are the most abundant source contributing to the significant combinatorial background. The goal of this work is to study how and if the CBM-Micro Vertex Detector could help to reduce background in the dielectron analysis.

# Contents

<b>Contents</b>	<b>1</b>
<b>List of Figures</b>	<b>3</b>
<b>List of Tables</b>	<b>7</b>
<b>1 Introduction</b>	<b>9</b>
1.1 Quantum Chromo Dynamics . . . . .	9
1.1.1 The QCD Lagrangian . . . . .	9
1.1.2 Symmetries . . . . .	10
1.1.3 Phases in QCD . . . . .	11
1.2 Dileptons . . . . .	12
1.2.1 In-Medium Modifications . . . . .	13
1.2.2 Experimental Results . . . . .	13
<b>2 The CBM Detector</b>	<b>17</b>
2.1 The Micro Vertex Detector (MVD) . . . . .	19
2.2 The Silicon Tracking Stations (STS) . . . . .	19
2.3 The Dipole Magnet . . . . .	19
2.4 The Ring Imaging Cherenkov Detector (RICH) . . . . .	20
2.5 The Transition Radiation Detector (TRD) . . . . .	21
2.6 The Time-of-Flight Wall (TOF) . . . . .	21
2.7 The Muon Chamber (MuCh) . . . . .	21
2.8 The Electromagnetic Calorimeter (ECAL) . . . . .	21
2.9 The Projectile Spectator Detector (PSD) . . . . .	22
<b>3 Analysis</b>	<b>23</b>
3.1 Simulation Setup . . . . .	23
3.2 Track Reconstruction . . . . .	23
3.2.1 L1 Reconstruction . . . . .	25
3.2.2 Global Tracking . . . . .	26
3.3 Particle Identification . . . . .	27
3.4 Characteristics of the Background . . . . .	36
3.5 Possible Role of the MVD . . . . .	40

3.6	Background Rejection . . . . .	41
3.6.1	KFParticle . . . . .	41
3.6.2	Photon Conversion Cut . . . . .	42
3.6.3	Primary Vertex Cut . . . . .	42
3.6.4	Track Topology Cut . . . . .	44
3.7	Failed Strategies for Background Rejection . . . . .	47
3.7.1	Hit Topology Cut . . . . .	47
3.7.2	Transverse Momentum Cut . . . . .	47
3.7.3	Photon Vertex Reconstruction in the MVD . . . . .	49
3.8	Results of the Analysis . . . . .	57
3.8.1	Ideal PID . . . . .	58
3.8.2	Realistic PID . . . . .	62
3.8.3	Delta Electrons . . . . .	62
3.8.4	Magnetic Field Strength . . . . .	66
<b>4</b>	<b>Summary</b>	<b>69</b>
	<b>Bibliography</b>	<b>74</b>

# List of Figures

1.1	Schematic phase diagram of strongly interacting matter as a function of temperature $T$ and baryon chemical potential $\mu$ [11]. . . .	12
1.2	CERES results for dielectron invariant mass after subtraction of the hadronic cocktail for Pb+Au collisions at 158 AGeV. Predictions from a broadening mass scenario are compared to a dropping $\rho$ mass (left) and a broadening mass excluding baryonic effects (right) [3]. . . . .	14
1.3	Acceptance-corrected invariant mass spectrum of the excess dimuons in Indium-Indium collisions at 158A GeV measured by NA60. Also shown are theoretical predictions by Rupert et al [32], Rapp/van Hess [38] and Dusling/Zahed [15]. Image taken from [35]. . . . .	15
1.4	Left: Comparison of the Ar+KCl invariant mass distribution with an isospin-averaged reference from p+p and n+p data. Right: Ratio of the heavy ion mass distributions (Ar+KCl and C+C) to the $1/2$ [pp+np] reference. Measured by HADES [7]. . . . .	15
2.1	3D model of the HADES and CBM detectors. . . . .	18
2.2	The magnetic field strength of the CBM magnet along the beam axis [28]. The target is located at $z = 50\text{cm}$ . . . . .	20
3.1	Invariant mass distribution of the Pluto cocktail used for central Au+Au collisions at 8A GeV. . . . .	24
3.2	Illustration of the cellular automaton on a simple example. Tracklets are created, linked and assigned a counter. In the final step tracklets are combined into a track candidate. . . . .	25
3.3	Output of the RICH neural network (RICH ANN). . . . .	28
3.4	Output of the TRD neural network (TRD ANN). . . . .	29
3.5	Relativistic velocity $\beta$ over momentum in the TOF for electrons and background of particles that have been identified as electrons in the RICH. . . . .	30
3.6	ROC curve of different TMVA classifiers used for electron identification. . . . .	31

3.7	The decision tree for the case where RICH, TRD and TOF information is available. . . . .	32
3.8	Remaining number of electrons and background tracks after each PID step. . . . .	33
3.9	This plot shows the Monte-Carlo ID of tracks where the reconstructed track (class StsTrack) and the track associated with the RICH ring are not matched to the same Monte-Carlo track (class MCTrack). Cuts for particle identification in the RICH, TRD and TOF detectors have been applied. Numbers are normalized per event. . . . .	34
3.10	Particle type of tracks that were either falsely identified as electrons or mismatches between reconstructed tracks and rings in the RICH. . . . .	34
3.11	Electron identification efficiency for all reconstructed electron tracks when asking for acceptance in the PID detectors only (left) and when using real PID. . . . .	35
3.12	Track types of positrons (columns) and electrons (rows) from in-medium $\rho$ decays that belong to the same pair. The ideal case of a fully identified pair is met by 3% of all tracks in the acceptance. The sum of all pairs adds to 1. . . . .	36
3.13	Track types of positrons (columns) and electrons (rows) from photon conversion that belong to the same pair. The sum of all pairs adds to 1. . . . .	37
3.14	Track types of positrons (columns) and electrons (rows) from $\pi^0$ -Dalitz decays that belong to the same pair. The sum of all pairs adds to 1. . . . .	38
3.15	Invariant mass of dielectrons from $\gamma$ -conversion, $\pi^0$ -Dalitz decays, signal and of the combinatorial background. The signal source is only the in-medium $\rho$ . . . . .	39
3.16	Momentum of electrons and positrons from different sources for accepted and reconstructed tracks. For the reconstructed tracks the momentum of the corresponding Monte-Carlo track is plotted. The signal source is the in-medium $\rho$ . . . . .	40
3.17	The reconstruction efficiency with and without the MVD for tracks from the target region. . . . .	41
3.18	The reconstructed z-vertex of $\gamma$ -conversions found with the KFParticleFinder per event. . . . .	42
3.19	The z-position of the reconstructed vertex, $\chi^2$ of the fit, reconstructed mass of the mother particle reconstructed with KFParticle and the opening angle between the daughter particles. . . .	43
3.20	Quality of the fit to the primary vertex with the MVD (upper row) and without the MVD (lower row). The cutoff values to separate electrons from $\pi^0$ -Dalitz and $\gamma$ -conversions that come from the primary vertex and those that are produced outside the target region were chosen based on the significance of the $\chi$ -distribution. . . . .	45

3.21	The z-position of the start vertex of all $\gamma$ -conversions in the acceptance and that remain after particle identification and the primary track cut. . . . .	46
3.22	The estimated x- and y-Position of tracks extrapolated to the first MVD station. A large portion of tracks from the primary vertex region pass the MVD through its inner hole at $ x  \leq 5\text{ mm}$ and $ y  \leq 5\text{ mm}$ . . . . .	46
3.23	The z-position of the start vertex of all $\gamma$ -conversions that remain after particle identification, the primary track cut and after extrapolation to the first MVD station. . . . .	47
3.24	Tracks are extrapolated to the primary vertex. Shown is the radial distance to the primary vertex with the MVD (upper row) and without the MVD (lower row) in the setup. The cutoff values to separate electrons that come from the primary vertex and those that are produced outside the target region were chosen based on the significance. . . . .	48
3.25	Signal-to-background in the mass range of $0.55\text{ GeV}/c^2 - 1.2\text{ GeV}/c^2$ when applying the primary vertex cut using either the $\sqrt{\chi^2}$ or radial distance value. . . . .	49
3.26	Comparison of the track topology for signal (in-medium $\rho$ ) and background tracks. . . . .	50
3.27	Significance for different cut values of the track topology cut. . .	51
3.28	Top row: the distance of a hit from a $\gamma$ -conversion and signal (in-medium $\rho$ ) to the nearest hit that does not belong to a reconstructed track. Also plotted is the distance of the true partners in the first MVD station. Bottom row: Momentum of the identified electron vs. distance to the nearest hit on the first MVD station for signal and $\gamma$ -conversion decays. Full field is applied. . . . .	52
3.29	Top row: the distance of a hit from a $\gamma$ -conversion and signal (in-medium $\rho$ ) to the nearest hit that does not belong to a reconstructed track. Also plotted is the distance of the true partners in the first MVD station. Bottom row: Momentum of the identified electron vs. distance to the nearest hit on the first MVD station for signal and $\gamma$ -conversion decays. The field has been reduced to 70%. . . . .	53
3.30	Transverse momentum distribution for different sources. Only tracks remaining after the track topology cut are shown. . . . .	54
3.31	Candidate finding efficiency of LitTrack for electron tracks that have at least three points in the MVD. Ideal seeds from the Monte Carlo track were used. Curling tracks are included. . . . .	54



3.32	Left: Amount of search candidates divided by fragments. Both terms refer to $e^+/e^-$ pairs from conversions where one particle was reconstructed and has a rich ring attached to it. The decay partner is called a fragment if it was not reconstructed, but the corresponding Monte Carlo track produced at least one hit in the MVD or STS. It is called a candidate if it has produced at least three hits in different MVD or STS stations. Right: The momentum of the track candidate to find versus the momentum of its identified track. . . . .	55
3.33	Invariant mass versus opening angle of the input pairs for LitTrack. . . . .	55
3.34	Momentum error of the track seed. . . . .	56
3.35	Left: Track finding efficiency versus momentum. Right: Amount of tracks where the correct hits, wrong hits or no hits have been attached. . . . .	56
3.36	Left: Track finding efficiency versus momentum. Right: Amount of tracks where the correct hits, wrong hits or no hits have been attached. The Monte Carlo momentum was smeared by 10% and used as the initial momentum guess for the track finder. . . . .	57
3.37	The invariant mass spectrum with the combinatorial background and contributions from different sources. Ideal PID has been used. . . . .	59
3.38	The signal-to-background ratio after each cut step. The MVD is included in the setup. Ideal PID has been used. . . . .	60
3.39	The invariant mass spectrum before and after the primary vertex cut. The invariant mass has been calculated with the reconstructed momentum in the upper row and with the Monte Carlo momentum in the lower row. Ideal PID has been used. . . . .	61
3.40	Comparison of signal-to-background, signal efficiency and significance with and without the MVD in the setup for ideal particle ID. . . . .	62
3.41	Comparison of signal-to-background, signal efficiency and significance with and without the MVD in the setup for realistic particle ID. . . . .	63
3.42	The detection efficiency of dielectrons from the low mass vector mesons sources with ideal and realistic particle identification. . . . .	64
3.43	The track topology cut for signal and background sources with and without $\delta$ -electrons. Ideal PID has been used. . . . .	67
4.1	Vergleich von Signal zu Untergrund, Signaleffizienz und Signifikanz mit und ohne dem MVD im Geometriesetup für realistische Teilchenidentifikation. . . . .	73

# List of Tables

1.1	Properties of light vector mesons [40] [29]. . . . .	13
1.2	Branching ratios and multiplicities for different dielectron sources [29]. . . . .	13
3.1	Assumed branching ratios and multiplicities for the dielectron cocktail. Multiplicities for $\omega$ and $\phi$ are from HSD calculations and the branching ratios from PDG [29]. The numbers for the branching ratio times multiplicity of the in-medium $\rho$ and QGP radiation are based on calculations for 25A GeV Au+Au [33]. The number has been scaled by the factor of 2 in the pion production difference observed in 8A GeV Au+Au and 25A GeV Au+Au UrQMD simulations [10]. . . . .	24
3.2	The electron identification cut sets applied for the RICH, TRD and TOF detectors. . . . .	30
3.3	Number of correctly identified electrons/positrons, falsely identified electrons/positrons and mismatches per event for the different cut sets. . . . .	31
3.4	Results of the dielectron analysis after all analysis cuts are applied. Three Million events were simulated with only the in-medium $\rho$ embedded. Numbers are for the mass region $0.55 \text{ GeV}/c^2 \leq m_{inv} \leq 1.2 \text{ GeV}/c^2$ . . . . .	33
3.5	Number of dielectron pairs in the acceptance from different background sources. . . . .	37
3.6	Results of the dielectron analysis when using the $\sqrt{\chi^2}$ or radial distance value as cut value for the primary vertex cut for the mass range of $0.55 \text{ GeV}/c^2$ to $1.2 \text{ GeV}/c^2$ . . . . .	46
3.7	Comparison of setups with and without the MVD included. Ideal PID has been used. . . . .	58
3.8	Comparison of setups with and without the MVD included. Realistic PID has been used. . . . .	63
3.9	Number of partially and fully identified pairs after particle identification for different PID methods and detector setups. . . . .	64

3.10	Comparison of setups without the MVD, with the MVD but without $\delta$ -electrons and finally with the MVD and $\delta$ -electrons added. The simulations only had in-medium $\rho$ embedded. Results are for the relevant mass range of $0.55 \text{ GeV}/c^2 \leq m_{inv} \leq 1.2 \text{ GeV}/c^2$ . .	66
3.11	Analysis results for different values of magnetic field strength in the invariant mass range of 0.55 GeV to 1.2 GeV. Included are only dilepton decays from the in-medium $\rho$ . . . . .	68
3.12	The number of dielectron decays from $\gamma$ -conversions where particle identification for at least one lepton is available. The partner may be either identified as well, only reconstructed in the MVD and STS or not reconstructed at all. . . . .	68

# Chapter 1

## Introduction

### 1.1 Quantum Chromo Dynamics

#### 1.1.1 The QCD Lagrangian

Quantum Chromo Dynamics (QCD) is the theory of the strong interaction and describes quarks, gluons and their interactions. There are six different types of quarks, called flavours. Quarks carry spin, fractional electric charges and a strong charge which comes in three variants referred to as colours. Quarks interact with each other via the vector gauge bosons of the strong force called gluons. As the gluons themselves carry a colour charge they can interact among each other as well. Eight gluons exist corresponding to the various elementary ways to transform one color into another.

The QCD Lagrangian is given by

$$\mathcal{L} = -\frac{1}{4}G_{\mu\nu}^a G_{\mu\nu}^a + \sum_f^{N_f} \bar{q}_f (i\gamma^\mu D_\mu - m_f) q_f. \quad (1.1)$$

where

$$G_{\mu\nu}^a = \partial_\mu A_\nu^a - \partial_\nu A_\mu^a + gf^{abc}A_\mu^b A_\nu^c \quad (1.2)$$

is the QCD field strength tensor and  $f^{abc} = 4i\text{Tr}([\lambda^a\lambda^b]\lambda^c)$  is a set of numbers called the SU(3) structure constants. The field vector  $A_\mu^a$  labeled by an adjoint color index  $a = 1 \dots 8$  describes the gluons. The covariant derivative acting on the quark fields is

$$iD_\mu q = \left( i\partial_\mu + gA_\mu^a \frac{\lambda^a}{2} \right) q \quad (1.3)$$

and  $m_f$  is the mass of the quark flavours. Besides the quark masses the dimensionless coupling constant  $g$  is the parameter for the QCD Lagrangian. At leading order it depends on the QCD scale parameter  $\Lambda_{QCD}$ :

$$g^2(q^2) = \frac{16\pi^2}{b_0 \log(q^2/\Lambda_{QCD}^2)}, \quad b_0 = \frac{11}{3}N_c - \frac{2}{3}N_f \quad (1.4)$$

where  $q$  is a characteristic momentum,  $N_f$  the number of active flavours and  $N_c = 3$  the number of colors. The coupling decreases with increasing momentum or translating this to configuration space it vanishes at short distances. This property of QCD is called asymptotic freedom and is the reason why it is expected that quarks and gluons will become free forming a plasma at high temperatures. On the other hand the coupling increases with decreasing momentum which leads to confinement.

### 1.1.2 Symmetries

A symmetry is a property of a system that leaves it invariant under certain transformations. Symmetries can be either exact or approximately realized if small violations of the consequences from the symmetry can be observed. If both the interaction which governs the system and the physical ground state obeys the symmetry then the system is in the Wigner-Weyl phase. On the other hand, if only the interaction is invariant, but not the physical state, it is in the Nambu-Goldstone phase. The symmetry is then called “hidden” or “spontaneously broken”. For a continuous symmetry that is broken a massless state called the Goldstone mode exists. For an approximately realized symmetry, also called explicitly broken symmetry, the Goldstone modes are not massless, but light. Finally, a symmetry might exist only for the classical interaction, but not on the quantum level. It is then called an “anomaly”.

An order parameter is a measure of the degree of order across the boundaries in a phase transition system. It is non-vanishing when a symmetry is broken and vanishes when the symmetry is restored.

A classical example is a ferromagnet: The spin-spin interaction is invariant under rotations. A critical point exists called the Curie point. Above the Curie temperature the system is in the Wigner-Weyl phase. However, below this temperature a physical state where all spins are aligned is preferred. The rotational symmetry is broken on a macroscopic scale and the system is in the Nambu-Goldstone phase. The order parameter of this symmetry transition is the magnetization. In case an external magnetic field is applied rotational symmetry is also explicitly broken from the start [18].

### Symmetries in QCD

The symmetries in QCD lead to different phases in strongly interacting matter. An important symmetry is chiral symmetry. Mathematically, an object is chiral

if it is not the same as its mirror image. If a particle with spin  $1/2$  is rotated by 360 degrees then the phase of its quantum wave function is shifted. The shift goes in opposite direction for right- and left-chiral fermions. Weak interactions only affect left-chiral particles and right-chiral anti-particles.

Helicity is given by the projection of a particle's spin onto its momentum. It is right-handed if the sign of this projection is positive. Otherwise the helicity is left-handed. For massless particles the helicity and chirality are the same in any reference frame. The QCD Lagrangian conserves the number of left-handed and right-handed quarks. Fermions are always left-chiral and have left-handed helicity while anti-Fermions are right-chiral and have right-handed helicity.

For particles with a mass, chirality and helicity are no longer the same. Since massive particles move at velocities less than the speed of light there exists a reference frame where an observer could overtake the particle and the helicity of the particle is reversed. Helicity is no longer Lorentz-invariant unlike the chirality. Distinct chirality states now have components of both left-handed and right-handed helicities. Chirality is no longer conserved and the symmetry is explicitly broken.

The true ground state of QCD is not a vacuum at  $T = 0$  and  $\mu = 0$ , but a condensate of  $q\bar{q}$  pairs. This ground state does not preserve the amount of left-handed and right-handed quarks

$$\langle \bar{\psi}\psi \rangle = \langle 0 | \bar{\psi}_L \psi_R + \bar{\psi}_R \psi_L | 0 \rangle \neq 0 \quad (1.5)$$

which is a definition of an order parameter. The chiral symmetry is only approximate due to the finite bare quark masses. On top, the approximate symmetry is spontaneously broken by the condensate. The hadrons acquire a mass which is much larger than the intrinsic mass of their constituent quarks. Most of the mass of visible matter is a result of this spontaneous symmetry breaking. Unbroken chiral symmetry would imply that particles with opposite parity have the same mass. In reality, for example the  $a_1$  Meson ( $J^{PC} = 1^{+-}$ ) is around  $500 MeV$  heavier than its chiral partner, the  $\rho$  Meson ( $J^{PC} = 1^{--}$ ).

The Goldstone-Bosons which are the Pions, Kaons and the Eta, have a mass due to the explicit breaking of chiral symmetry, but are light compared to the nucleons.

### 1.1.3 Phases in QCD

The symmetries of QCD and asymptotic freedom lead to a rich phase diagram of strongly interacting matter. Figure 1.1 shows a sketch of the predicted phases in QCD as a function of temperature and baryon chemical potential.

At temperatures and chemical potentials of zero the coupling between quarks is large as the interactions are dominated by large distances. Quarks and gluons are confined into hadrons. Goldstone bosons exist due to chiral symmetry breaking.

At high temperatures quarks and gluons have large momenta and the interaction is expected to be weak due to asymptotic freedom. These particles form a plasma of mobile charges called the quark gluon plasma (QGP). Quarks and

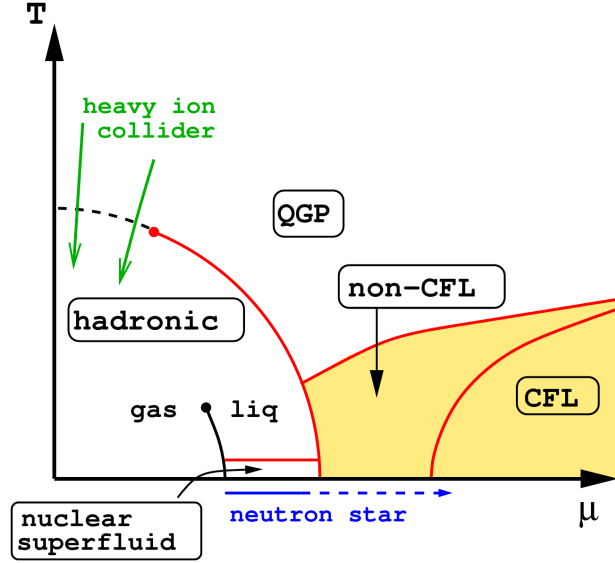


Figure 1.1: Schematic phase diagram of strongly interacting matter as a function of temperature  $T$  and baryon chemical potential  $\mu$  [11].

gluons are no longer confined and chiral symmetry is restored. This implies a phase transition between the plasma and hadronic phase whose properties depend on the masses of the quarks. The phase transition is expected to happen at temperatures around 150 MeV. It can be of first or second order for massless  $u$  and  $d$  quarks while it is a crossover for realistic quark masses. The transition is believed to strengthen as a function of chemical potential, so that there is a critical point where the crossover turns into a first order phase transition. This point is the critical endpoint of the chiral phase transition [11].

Quarks and gluons are also weakly coupled at large chemical potentials and low temperatures. Attractive interactions between quark pairs lead to color superconductivity and the formation of a  $\langle qq \rangle$  condensate. The favoured phase in three flavour quark matter is called the colour-flavour-locked phase.

## 1.2 Dileptons

Dileptons are produced in the decay of time-like virtual photons into an  $e^+e^-$  or  $\mu^+\mu^-$  pair. As these particles are not subject to the strong force their mean free path is much larger than the system size of a heavy ion collision. Of special interest are the light vector mesons  $\rho$ ,  $\omega$  and  $\phi$  that have an exclusive decay channel into dileptons and their lifetime is short enough so that a considerable fraction of decays occur in the hot and dense phase of heavy ion collisions (see table 1.1). This makes dileptons good probes and their measurements could provide rich information on the onset of deconfinement, on the subject of chiral

Vector Meson	$m$ [MeV/c]	$\Gamma$ [MeV]	$\tau$ [fm/c]
$\rho$	$775.26 \pm 0.25$	$149.1 \pm 0.8$	1.3
$\omega$	$782.65 \pm 0.12$	$8.49 \pm 0.08$	23
$\phi$	$1019.461 \pm 0.019$	$4.266 \pm 0.031$	44

Table 1.1: Properties of light vector mesons [40] [29].

Source	Multiplicity	Decay Channel	Branching Ratio $\rightarrow e^+e^-$
$\rho$	9	$e^+e^-$	$(4.72 \pm 0.05) \cdot 10^{-5}$
$\omega$	19	$e^+e^-$	$(7.28 \pm 0.14) \cdot 10^{-5}$
		$\pi^0 e^+e^-$	$(7.7 \pm 0.6) \cdot 10^{-4}$
$\phi$	0.12	$e^+e^-$	$(2.954 \pm 0.030) \cdot 10^{-4}$
$\pi^0$	221	$\gamma e^+e^-$	$(1.174 \pm 0.035) \cdot 10^{-2}$
$\eta$	16	$\gamma e^+e^-$	$(6.9 \pm 0.4) \cdot 10^{-3}$

Table 1.2: Branching ratios and multiplicities for different dielectron sources [29].

symmetry restoration and may reveal information on the characteristics of the matter created in the collisions.

The challenge for measuring dielectrons are the small branching ratios which are of the order of the electromagnetic coupling constant  $\alpha_{em} = 1/137$  squared and the background mainly produced by  $\pi^0$ -Dalitz decays and photon conversions (table 1.2).

### 1.2.1 In-Medium Modifications

Chiral symmetry restoration implies that the spectral functions of chiral partners like the  $\rho$  and  $a_1$  become equal at large chemical potentials and temperatures. Possible realizations include a dropping mass and broadening mass scenario.

An in-medium dropping  $\rho$  mass was introduced by Brown and Rho [12]. In the limit of vanishing quark masses the mass of hadrons is produced by the chiral condensate  $\langle \bar{q}q \rangle$ . With a reduced chiral condensate the mass of the  $\rho$  is expected to decrease.

An alternative scenario is the mixing of the spectral functions of the  $\rho$  and  $a_1$  meson [14] or a mixing of the  $\rho$  meson with hadronic states, mostly excited baryons [30] which would result in a broadening of the mass.

### 1.2.2 Experimental Results

The first dilepton invariant mass measurements done by the CERES collaboration [2] [3] showed an enhancement below the  $\rho$  mass peak (figure 1.2). The data



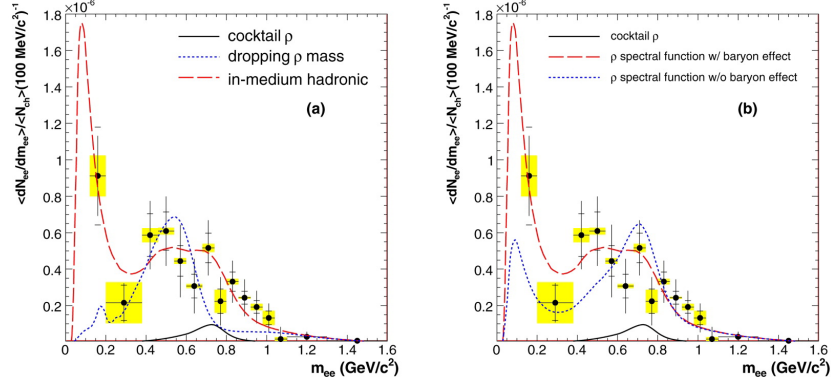


Figure 1.2: CERES results for dielectron invariant mass after subtraction of the hadronic cocktail for Pb+Au collisions at 158 AGeV. Predictions from a broadening mass scenario are compared to a dropping  $\rho$  mass (left) and a broadening mass excluding baryonic effects (right) [3].

was consistent with in medium modifications of the  $\rho$  but could not distinguish between the dropping mass and broadening mass scenarios.

Further dimuon measurements by the NA60 collaboration at CERN SPS [9] [8] ruled out the dropping mass scenario while results are consistent with the broadening mass [31]. The acceptance-corrected invariant mass spectrum of the excess dimuons along with theoretical calculations for in-medium broadening of the  $\rho$  mass is shown in figure 1.3. The calculations from van Hees and Rapp [38] fit closest to the data. Those from Rupert et al [32] as well as Dusling and Zahed [15] only take leading order corrections of the temperature and density into account while Rapp and van Hees also consider higher order effects.

At lower energies dileptons have also been measured by HADES with C+C at 1 and 2 AGeV and Ar+KCl at 1.76 AGeV [4] [5] [6] [7]. An enhancement below the  $\rho$  mass could be observed (figure 1.4).

The STAR experiment at RHIC confirmed an enhancement below the  $\rho$  mass peak in measurements for several beam energies between  $\sqrt{s} = 19.6 \text{ GeV}$  and  $\sqrt{s} = 200 \text{ GeV}$  [39]. Dilepton spectra for the low end of the CERN SPS energies are also available [1].

The structure of the QCD phase diagram for moderate temperatures and high baryon chemical potentials accessible in the planned SIS100 accelerator at FAIR and the CBM experiment is still practically unexplored.

The intermediate dilepton mass region between 1 GeV and 3 GeV may give access to the thermal QGP radiation. The main background sources in this region originate from pairs from Drell-Yan production and semi-leptonic decays of open charm pairs. Figure 1.3 shows the dilepton mass in the intermediate measured by NA60 after the background has been removed. An exponential fall-off that is consistent with a temperature of  $T = (205 \pm 12) \text{ MeV}$  for the thermal radiation can be seen [8] [35] which is higher than the critical temperature

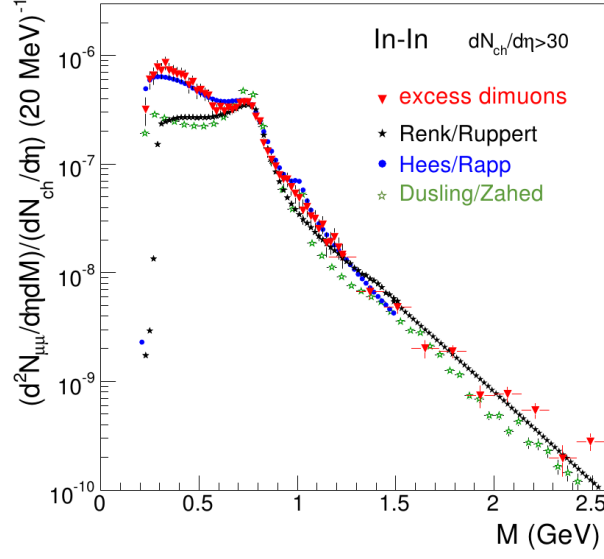


Figure 1.3: Acceptance-corrected invariant mass spectrum of the excess dimuons in Indium-Indium collisions at 158A GeV measured by NA60. Also shown are theoretical predictions by Rupert et al [32], Rapp/van Hess [38] and Dusling/Zahed [15]. Image taken from [35].

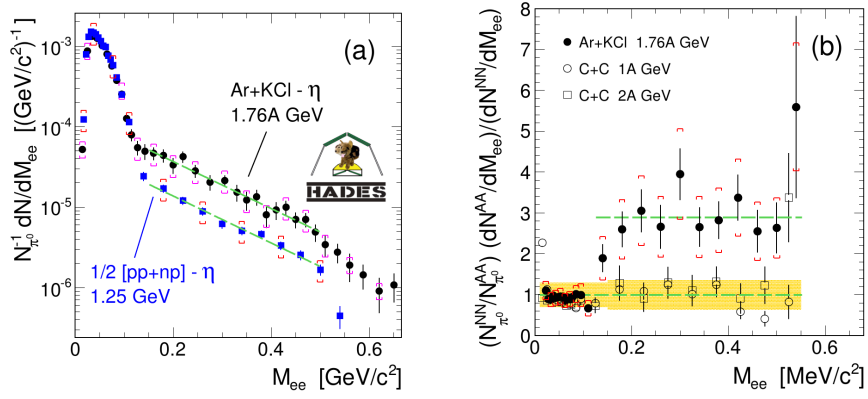


Figure 1.4: Left: Comparison of the Ar+KCl invariant mass distribution with an isospin-averaged reference from p+p and n+p data. Right: Ratio of the heavy ion mass distributions (Ar+KCl and C+C) to the  $1/2[pp+np]$  reference. Measured by HADES [7].

$T_C \simeq 150 \text{ MeV}$  predicted by QCD. [11]

## Chapter 2

# The CBM Detector

The Compressed Baryonic Matter (CBM) experiment is going to be operated at the Facility for Antiproton and Ion Research (FAIR) located in Darmstadt, Germany. The SIS100 synchrotron is going to have a rigidity of 100 Tm. The available kinetic beam energy depends mainly on this bending power  $B \cdot r$ :

$$\frac{E}{A} \simeq \sqrt{(0.3 \cdot B \cdot r \cdot Z/A)^2 + m^2} - m \quad (2.1)$$

First beams delivered from SIS100 are scheduled for the year 20018<sup>1</sup>. Heavy ion beams in the range between 2 and 14 A GeV allow the investigation of matter in the vicinity of the phase boundary.

The CBM experiment has been designed for the measurement of bulk and rare probes:

- Particles with charm quarks are created in the very first stages of a heavy ion collision. A global  $m_T$ -scaling of mesons, especially those with strange and charm quarks, indicates in-medium modifications which may be related to effects of chiral symmetry restoration. Changes of charm particle ratios such as  $\Psi'/(J/\psi)$  and  $(J/\psi)/D$  as a function of beam energy may indicate the crossing of the phase boundary.
- Dilepton measurements could provide a rich information on the onset of deconfinement and on the subject of chiral symmetry restoration. The light vector mesons  $\rho$ ,  $\omega$  and  $\phi$  are known to be excellent probes of the strongly interacting matter under extreme conditions. The leptonic decay channels of these mesons are of special interest as the leptons leave the hot and dense fireball without strong interaction and may reveal information on the characteristics of the matter created in the collisions.
- The strength of the elliptic flow  $v_2$  measured as a function of transverse momentum for various particle species reflects the initial pressure of the

---

<sup>1</sup>[18], A4 Version, Part V, chapter 1.2., page 614.

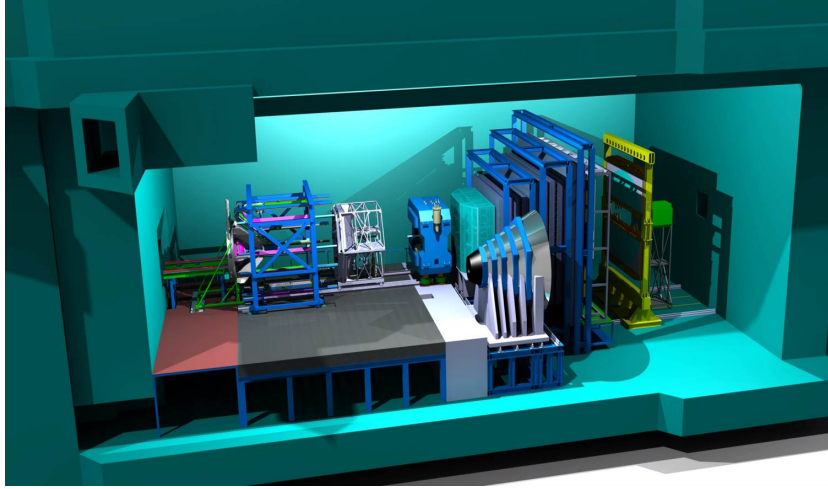


Figure 2.1: 3D model of the HADES and CBM detectors.

system. The vanishing of directed flow at a certain beam energy would indicate a strong softening of the equation of state.

- Fluctuations of the kaon, pion and proton multiplicities, in particular of their higher moments, measured as a function of beam energy, are expected to be sensitive indicators for the location of the critical point.
- Hypernuclei allow for studying the evolution of nuclear structure into the yet unexplored territory of the nuclear chart and to determine the properties of many short-lived nuclei which are produced in explosive astrophysical events. The yields, spectra and collective flow of strange hyperons are sensitive diagnostic probes of the early and dense fireball, and, therefore, are prime observables in heavy-ion collisions at SIS100.

The CBM detector is going to measure protons, pions, kaons, hyperons, hadronic resonances, light vector mesons, charmonium and open charm. It has to provide hadron and lepton identification. Different setups will exist to measure either electrons or muons. In order to deal with the low cross section for charm production and low branching ratios for the dilepton decay channels of low mass vector mesons the measurements are performed at high interaction rates requiring fast and radiation hard detectors. Since the FAIR accelerators will provide a continuous beam instead of a bunched one fast online event reconstruction and selection is an important requirement. The polar acceptance of the detector lies between  $2.5^\circ$  and  $25^\circ$ . A 3-D model of the CBM detector is shown in fig. 2.1.

## 2.1 The Micro Vertex Detector (MVD)

Open charm mesons are produced early in heavy ion collisions and have a lifetime of  $c\tau = 123\,\mu\text{m}$  ( $D^0/\bar{D}^0$ ) and  $312\,\mu\text{m}$  ( $D^+/D^-$ ). Reconstructing the decay vertex of these particles requires a detector with high position resolution, a low material budget to reduce multiple scattering and high radiation hardness. The targeted material budget is  $x/x_0$  of 0.3% for the first and 0.5% for the other stations where  $x/x_0$  is the track length  $x$  in units of the material's radiation length  $X_0$ . The MVD can also be used for track reconstruction in addition to the STS which may help for dielectron analysis.

These requirements are met by Monolithic Active Pixel Sensors (MAPS). At the bottom of a pixel cell is a heavily doped silicon substrate over which a p-doped epitaxial layer is grown which is also the sensing volume. Located on top of this layer are P- and N-wells. The P-wells contain circuitry while the N-wells serve as detecting elements. A small voltage is applied to the N-well diode resulting in a depleted region in the epitaxial layer. Electron-hole pairs are generated by the passage of charged particles. The electrons are confined within the epitaxial layer by the substrate until they reach the depleted zone and are absorbed by the N-well diodes. This structure is repeated creating a pixel matrix.

The detector will be operated in a vacuum chamber to prevent multiple scattering before particles reach the MVD stations. The first MVD station is placed as close to the target as possible to ensure a good secondary vertex resolution. The last two MVD stations are placed as close to the STS as possible to improve the assignment of hits in the MVD to tracks reconstructed in the STS [37]. Due to the expected radiation dose the acceptance of the first MVD station has a smaller polar angle coverage [36].

## 2.2 The Silicon Tracking Stations (STS)

The STS is the main detector for track reconstruction and momentum determination. The momentum resolution is required to be of the order of 1%. Such a performance can only be achieved with a low material budget. The electronics, cooling and mechanical infrastructure are located outside the detector acceptance. Eight layers with silicon microstrip sensors are placed between 30 cm and 100 cm downstream inside the magnetic field. The sensors will be double-sided with a stereo angle of  $7.5^\circ$ , a strip pitch of  $58\,\mu\text{m}$ , strip lengths between 20 and  $60\,\text{mm}$  and a thickness of  $300\,\mu\text{m}$  of silicon. To improve reconstruction of low momentum electrons the first five stations cover an extended range in horizontal direction going beyond the required  $25^\circ$  polar acceptance [23].

## 2.3 The Dipole Magnet

The CBM magnet provides a maximum magnetic field integral of 1 Tm. It houses the MVD and STS systems [28]. Figure 2.2 shows the field strength

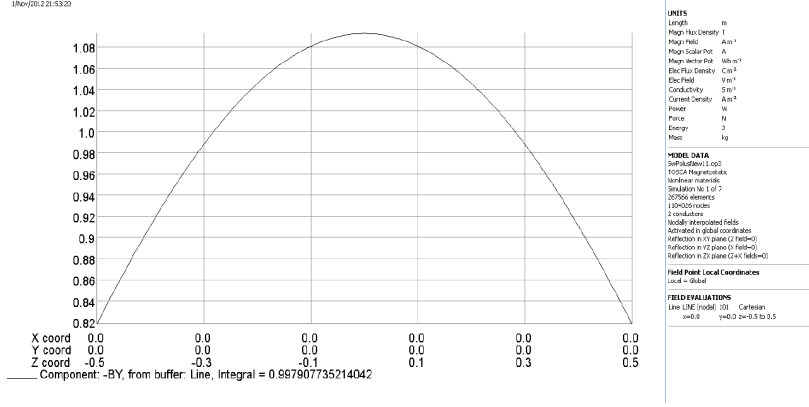


Figure 2.2: The magnetic field strength of the CBM magnet along the beam axis [28]. The target is located at  $z = 50\text{cm}$ .

along the beam axis. The field strength at the first MVD station is already 80% of its maximum value.

## 2.4 The Ring Imaging Cherenkov Detector (RICH)

The detectors for particle identification are located behind the magnetic field. The particles first reach the Ring Imaging Cherenkov (RICH) detector. They pass through a radiator gas with refraction index  $n$ . If the particle's velocity  $\beta$  is greater than the speed of light  $c/n$  in that medium then it emits Cherenkov light. The light cone is centred around the particle's trajectory and has an opening angle of  $\cos \Theta_C = 1/(\beta \cdot n)$ . The photons are reflected by a spherical glass mirror onto a photosensitive detector and focused to rings. The CBM-RICH will employ  $\text{CO}_2$  as radiator gas with a pion threshold for Cherenkov radiation of  $4.65 \text{ GeV}/c$ . Based on simulations the RICH detector alone yielded a pion suppression factor of 360 at an electron identification efficiency of 83% for momenta below  $12 \text{ GeV}$  at  $25 \text{ AGeV}$  beam energy and a pion suppression of 1400 at an identification efficiency of 87% for  $8 \text{ AGeV}$  beam energy. The pion suppression can be further improved with the TRD and TOF detectors. In-beam tests with a prototype have shown that 22 photons are measured per electron ring.

To recognize rings a local search of candidates is performed based on the Hough transform method. An artificial neural network is then used to reduce the amount of wrong rings using six parameters: the number of hits in a ring, the ring radius, the  $\chi^2$  of the circle fit, position of the ring on the photon detector plane, uniformity of the hit distribution on the ring and the number of hits in a small corridor around the ring [16].

## 2.5 The Transition Radiation Detector (TRD)

Transition radiation is emitted when charged particles move across the boundary of two media with different dielectric constants. The final CBM-TRD will consist of 9–10 detector layers grouped into three stations. For measurements at SIS100 only one station with 2–4 detector layers will be used. The TRD serves as tracking stations between the STS and TOF and as an additional detector for identification of electrons with momenta greater than  $1.5\text{ GeV}$ . Prototype gas detectors have been built and tested with particle rates of up to  $400\text{ kHz/cm}^2$  without deterioration of their performance [16].

## 2.6 The Time-of-Flight Wall (TOF)

The CBM-TOF wall will be built using Multigap Resistive Plate Counters (MRPC). An RPC is a gas detector that consists of two parallel electrode plates. An electric field is applied between the plates. The gap between the plates is filled with a counter gas that provides electrons by ionization and a quencher gas that absorbs photons. Charged particles trigger an electron avalanche causing a discharge. Due to the high resistivity of the electrodes and the photon absorbing quencher gas the discharge can't spread through the whole gas. Thus, the electric field is switched off in a limited area where the discharge occurred. In multigap RPCs the gas gap is divided by additional anode-cathode plates. This combines the good time resolution of a narrow gap with the higher rate capabilities and lower power dissipation of a wide gap.

The CBM-TOF wall will be placed  $10\text{ m}$  behind the primary target and covers an area of around  $120\text{ m}^2$ . It will be composed of six different types of modules and contain more than 50000 measuring cells. A time resolution of at least  $80\text{ ps}$  is required for the CBM physics cases. It is used for hadron identification [17].

## 2.7 The Muon Chamber (MuCh)

In CBM both dielectron and dimuon decay channels will be measured. To achieve this the RICH and the first TRD station can be exchanged for the muon detector. It consists of six hadron absorber layers made of carbon and iron plates. A triplet of gas tracking chamber will be located behind each absorber layer [13].

## 2.8 The Electromagnetic Calorimeter (ECAL)

A "shashlik" type calorimeter will be used to measure direct photons and photons from neutral meson decays. It will be of modular design with a total of 140 layers of lead and scintillator materials [23].



## 2.9 The Projectile Spectator Detector (PSD)

The PSD is a calorimeter which will be composed of 44 modules, each with 60 layers of lead and scintillator materials. The study of collective flow requires the determination of the reaction plane which can be achieved by measuring the spectator particles, i.e. particles that did not participate in the heavy ion collisions [22].

## Chapter 3

# Analysis

### 3.1 Simulation Setup

The simulations were performed for central Au+Au collisions with a beam energy of 8A GeV that will be available at the planned SIS-100. The hadronic environment was generated with the microscopic transport model UrQMD. The leptonic and Dalitz-decays of the  $\omega$  and  $\phi$  vector mesons were obtained using the Pluto event generator [19]. Dileptons from medium-modified  $\rho^0$  as calculated by Rapp and Wambach [31] as well as dileptons from QGP radiation have also been included in the Pluto cocktail [34]. One decay from Pluto has been embedded into each UrQMD event. The results are later appropriately rescaled by the branching ratio and multiplicity (table 3.1).

The  $\omega$  and  $\phi$  dilepton decay channels have been simulated with a fixed width Breit-Wigner mass distribution. The  $\omega$ -Dalitz decay also takes these deviations from the Breit-Wigner shape into account: a scale factor  $1/m^3$  to account for Vector Meson Dominance and a sampling of the total energy as a relativistic Boltzmann distribution ( $Ee^{-E/T}$ ). The invariant mass spectrum of the Pluto cocktail is shown in figure 3.1.

All particles are propagated through the detector system with the CBM software framework. The shown results are based on the NOV15 release candidate dated November 16, 2015. The CBM software offers seven standard geometry setups. The one intended for electron analysis at SIS-100 energies includes 4 MVD stations, 8 STS stations, the RICH, 4 stations of the TRD and the TOF detector. The MVD stations are located at  $z = 5, 10, 15$  and 20cm downstream of the target. Of special interest is how the MVD might contribute to the dielectron analysis.

### 3.2 Track Reconstruction

Track reconstruction is divided into two steps: The track finding and parameter estimation in the STS and optionally the MVD in the software package called

Source	Decay Channel	Multiplicity	Branching Ratio $\rightarrow e^+e^-$
$\omega$	$e^+e^-$	19	$7.28 \cdot 10^{-5}$
	$\pi^0 e^+e^-$		$7.7 \cdot 10^{-4}$
$\phi$	$e^+e^-$	0.12	$2.954 \cdot 10^{-4}$
Source	Decay Channel	Multiplicity *	Branching Ratio $\rightarrow e^+e^-$
In-medium $\rho$	$e^+e^-$		$2.25 \cdot 10^{-2}$
QGP Radiation	$e^+e^-$		$5.74 \cdot 10^{-3}$

Table 3.1: Assumed branching ratios and multiplicities for the dielectron cocktail. Multiplicities for  $\omega$  and  $\phi$  are from HSD calculations and the branching ratios from PDG [29]. The numbers for the branching ratio times multiplicity of the in-medium  $\rho$  and QGP radiation are based on calculations for 25A GeV Au+Au [33]. The number has been scaled by the factor of 2 in the pion production difference observed in 8A GeV Au+Au and 25A GeV Au+Au UrQMD simulations [10].

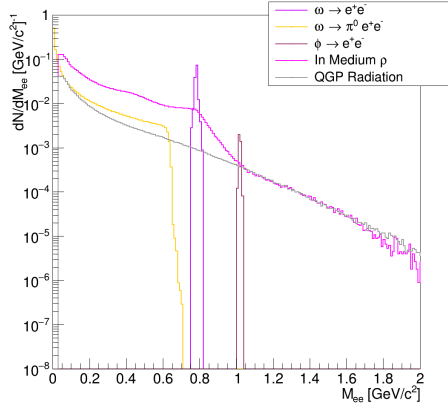


Figure 3.1: Invariant mass distribution of the Pluto cocktail used for central Au+Au collisions at 8A GeV.

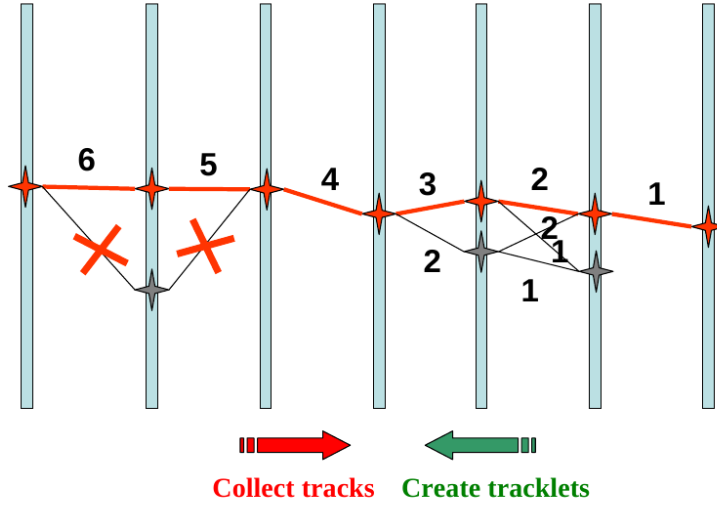


Figure 3.2: Illustration of the cellular automaton on a simple example. Tracklets are created, linked and assigned a counter. In the final step tracklets are combined into a track candidate.

L1. Rings in the RICH and hits in the TRD and TOF detectors are then attached with a track following method implemented in the software package called LitTrack.

### 3.2.1 L1 Reconstruction

#### Track Finding

The track finder is based on the cellular automaton. Figure 3.2 shows an illustration of the algorithm for a simple example. In a first step, short track segments called tracklets are created using all groups of neighbouring detector stations. The algorithm starts with the most downstream chamber and goes back in the direction onto the target. Cuts reflecting a geometrical acceptance of the detector system are applied to create only tracklets that are part of tracks with enough hits. The Kalman filter estimator is run on the tracklets and a cut on  $\chi^2$  is applied to reject arbitrary combinations of hits. Since hits in the detector stations are sorted, tracklets are generated in groups with the same z-position of its first hit. Every hit has a pointer to the first and last tracklet of its group.

Tracklets are then extrapolated to the next detector station in direction of the target applying a track model to the tracklets with a common point in order to find neighbours, i.e. possible track continuations according to the track model. Each tracklet has a counter representing its possible position on a track. If neighbours are found then the counter of the current tracklet is incremented

with respect to a neighbour with the largest counter.

In the next step tracklets are combined into track candidates. The algorithm starts with the tracklets that have the largest counter ( $\text{counter}^{\text{max}}$ ), takes a neighbour downstream whose counter is one less for each of these tracklets, continues further down following the counters making branches, but no empty layers and finally keeps the track with the best  $\chi^2$  for each initial tracklet. After this step a set of track candidates that have the same number of hits has been created. The candidates are sorted by their  $\chi^2$ . Starting with the track with the highest  $\chi^2$  it is checked if the number of used hits is less than a parameter  $N_{\text{max}}$  that depends on the track density. The hits of the track candidate are then flagged as used or the candidate is deleted. The algorithm repeats collecting tracks with decremented  $\text{counter}^{\text{max}}$  until the shortest tracks are collected.

In order to take detector inefficiencies into account short tracks are propagated through inefficient stations and lost hits using the track model are gathered. In addition short track segments are merged into long tracks to reduce the number of clones. Additional cuts are applied to kill ghost tracks [26] [23].

### Track Parameter Determination

Track and vertex fitting are performed with a Kalman filter based approach [25]. Propagation of tracks through the magnetic field is done with a specially developed formula [21]. The magnetic field in each detector station is approximated by a 4th order polynomial and the field between stations is approximated by a parabola. Its coefficients depend on the three closest hits of the current track. This way the algorithm can operate in the cache instead of accessing the large magnetic field map. Precision of all data has been reduced from double to single to optimize memory usage. The algorithm has been adapted for use of the SIMD (Single Instruction Multiple Data) instruction set for further speed increases [26].

### 3.2.2 Global Tracking

Hits in the PID detectors are attached to a reconstructed track with a track following method implemented in the software package called LitTrack. Tracks reconstructed in the STS by the L1 algorithm serve as seeds providing initial track parameters. They are extrapolated to the next detector station by a straight line outside of the magnetic field or a Runge-Kutta method of fourth order when passing through the magnetic field. Multiple scattering as well as energy loss by ionization and radiation are taken into account. After the propagation hits may be attached to the track. A validation gate  $v$  is calculated based on the covariance matrix  $C$  and the distance vector  $r$  between the extrapolated track and the hit:

$$v = rC^{-1}r^T. \quad (3.1)$$

A cut is applied on  $v$  to avoid assigning wrong hits. Two different methods for hit to track association exist: Either only the closest hit with the smallest  $v$  in

the validation gate is selected or a separate branch is created for each hit in the validation gate and the best branch is selected at the end. After possible hits are assigned the track parameters are updated with the Kalman filter formalism and the procedure is repeated for the next detector station.

After track finding the tracks are sorted by their quality based on track length and  $\chi^2$ . Tracks are rejected if the number of hits shared with other tracks exceed a cut value [27].

### 3.3 Particle Identification

High efficiency and purity of the identified electrons are necessary for good pair efficiency and background rejection in the dielectron analysis. A characteristic feature of pairs from  $\pi^0$ -Dalitz decays and photon conversions is the small opening angle. Unlike in other experiments that measure dielectrons like HADES the PID detectors of CBM are located behind the magnetic field and the main material budget. Pairs with small opening angles will be opened up before particle identification is available and additional background is to be expected due to partially identified  $\gamma$ -conversions produced in the MVD and STS.

To recognize rings a local search of candidates is performed based on the Hough transform method. An artificial neural network is then used to reduce the amount of wrong rings using six parameters: the number of hits in a ring, the ring radius, the  $\chi^2$  of the circle fit, position of the ring on the photon detector plane, uniformity of the hit distribution on the ring and the number of hits in a small corridor around the ring [16].

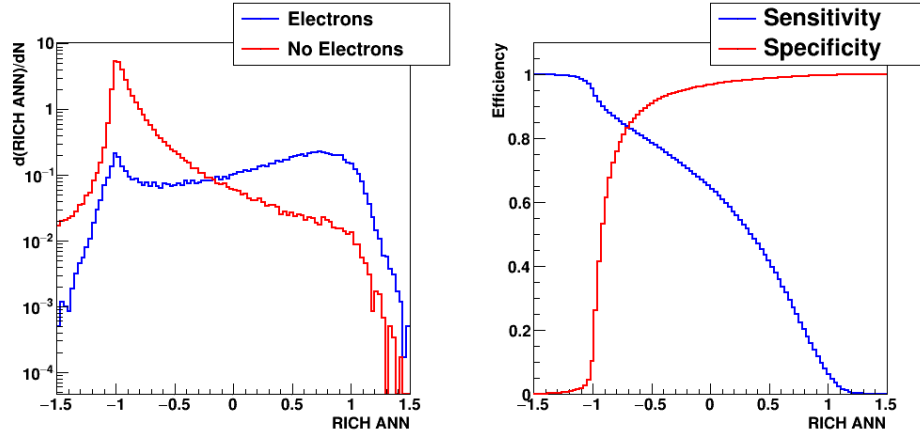
Rings from various background sources need to be identified and rejected to have a pure sample of identified electrons. Tracks from photon conversions in the MVD, STS or magnet yoke may not be fully reconstructed in the STS, but produce a ring in the RICH. Due to the high track density a RICH ring may be attached to the wrong reconstructed track. Hadrons, mostly pions, with high momenta may also produce rings in the RICH. Another background source are fake rings created from combinations of close hits.

The response of the neural network (RICH ANN) for true electrons and background is shown in figure 3.3. It produces continuous output values where ideally +1 would represent a good electron ring and -1 a background ring.

The energy loss information of the TRD can be used to further reduce background. As with the RICH a neural network is used in the TRD to discriminate electrons from background (figure 3.4).

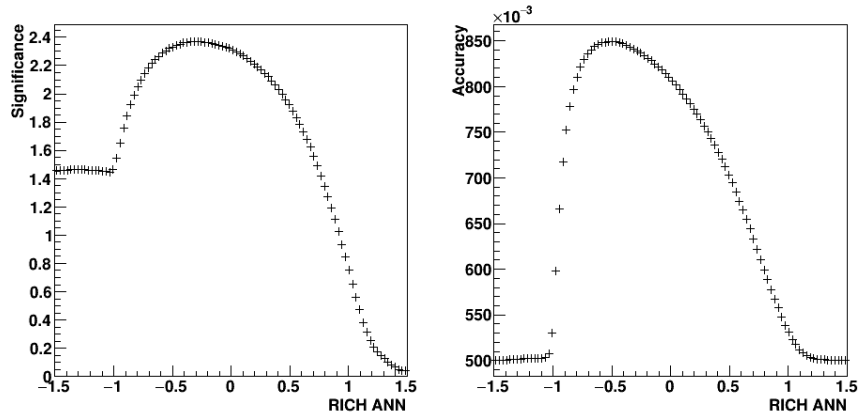
The time-of-flight can help to reduce mismatches of tracks in the STS and RICH rings and the number of pions and protons falsely identified as leptons. A cut depending on relativistic velocity  $\beta$  is applied (figure 3.5).

Four sets of PID cuts are compared: maximum significance, maximum accuracy, cuts that result in 90% electron identification efficiency and 80% electron identification efficiency in each detector. The significance is defined as  $S/\sqrt{S+B}$  where  $S$  is the number of correctly identified electrons/positrons and  $B$  the number of background tracks, i.e. particles that are not electrons/positrons,



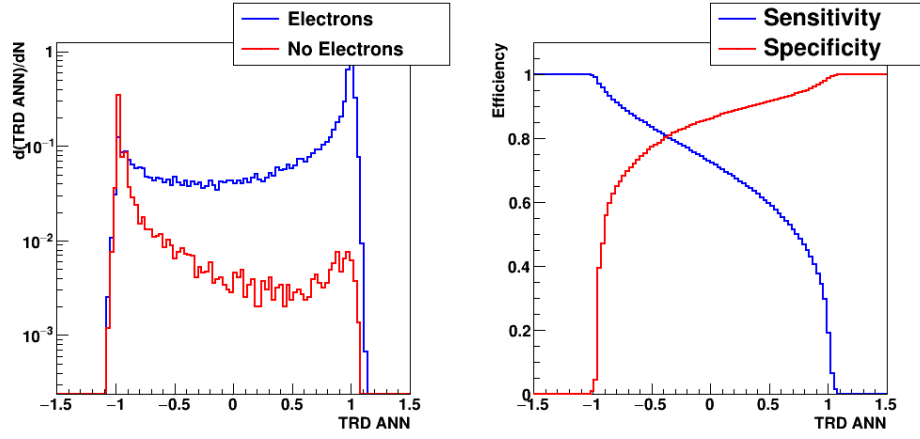
(a) Response function of the RICH neural network for electrons and other particles.

(b) Sensitivity (signal efficiency) and specificity (background rejection efficiency) of the RICH neural network.



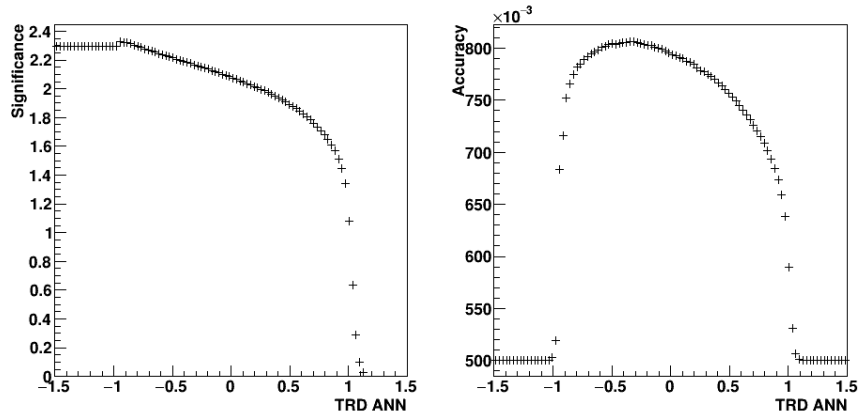
(c) Significance of the neural network response. (d) Accuracy of the neural network response.

Figure 3.3: Output of the RICH neural network (RICH ANN).



(a) Response function of the TRD neutral network for electrons and other particles.

(b) Sensitivity (signal efficiency) and specificity (background rejection efficiency) of the TRD neutral network.



(c) Significance of the neural network response. re-(d) Accuracy of the neural network response.

Figure 3.4: Output of the TRD neural network (TRD ANN).



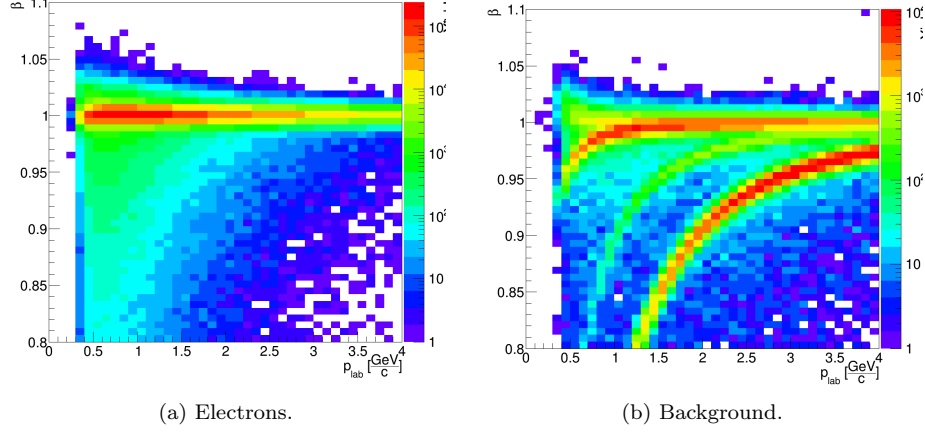


Figure 3.5: Relativistic velocity  $\beta$  over momentum in the TOF for electrons and background of particles that have been identified as electrons in the RICH.

PID Cuts	RICH ANN	TRD ANN	TOF $\beta$
Max. Significance	-0.3	-0.9	0.991
Max. Accuracy	-0.5	-0.33	0.997
90% Efficiency	-0.9	-0.75	0.996
80% Efficiency	-0.6	-0.45	0.998

Table 3.2: The electron identification cut sets applied for the RICH, TRD and TOF detectors.

but are wrongly identified as such, and mismatches a track reconstructed in the MVD and STS, and the track associated with a RICH ring are not matched to the same Monte-Carlo track. The accuracy is  $1/2(\text{sensitivity} + \text{specificity})$ . Information from the TRD and TOF detectors are used when available. The cut values are listed in table 3.2.

The Toolkit for MultiVariate Analysis (TMVA) [24] was also used for cut optimisation. TMVA is a software package for multivariate classification and regression. Several supervised learning algorithms are provided that use training samples for which the output is known to either find a decision boundary (classification) or approximate the functional behaviour defining the target value (regression). The learning methods include, among others, likelihood estimation, artificial neural networks and boosted decision trees. A decision tree is a binary tree structured classifier. On each node a yes/no decision is made on a single variable until a leaf node is reached. Decision trees are unstable with respect to fluctuations in the training sample. Boosting mitigates this problem by constructing several trees. An event is then classified by a plurality vote.

PID Cuts	True $e^+/e^-$	Wrong $e^+/e^-$	Mismatches
Max. Significance	1.32	0.0091	0.049
Max. Accuracy	1.06	0.0054	0.024
90% Efficiency	1.39	0.023	0.19
80% Efficiency	1.03	0.0072	0.030
TMVA	1.98	0.0031	0.35

Table 3.3: Number of correctly identified electrons/positrons, falsely identified electrons/positrons and mismatches per event for the different cut sets.

Figure 3.6 shows the receiver operating characteristic (ROC) of different classifiers. The training samples consisted of 60,000 electron and background tracks. The variables used for classification were the reconstructed momentum, number of RICH hits, RICH neural network, number of TRD hits, TRD neural network as well as mass and beta from the TOF. The boosted decision tree shows the best separation performance. Additional decision trees were trained for the cases where only information from the RICH and only information from the RICH and TRD detectors were available.

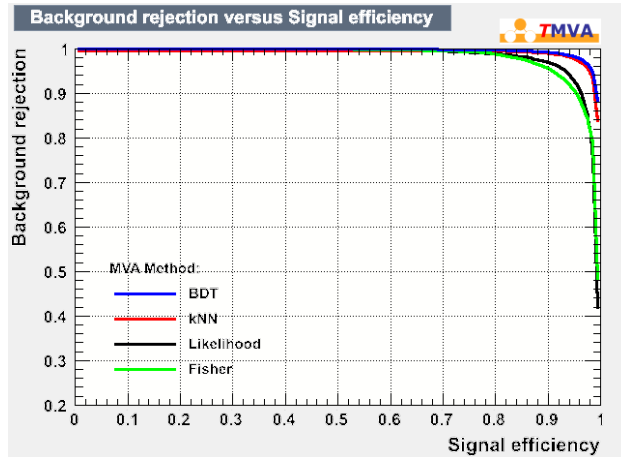


Figure 3.6: ROC curve of different TMVA classifiers used for electron identification.

Table 3.3 compares the electron identification performance for the different cut sets. Given are the numbers per event of correctly identified electrons, the number of particles misidentified as electrons and number of mismatches where a RICH ring was not attached to the correct reconstructed track.

Overall the TRD cut is effective at removing background (figure 3.8). The mismatches are mostly pion and proton tracks reconstructed in the STS that are attached to a RICH ring triggered by an electron or positron track (figure

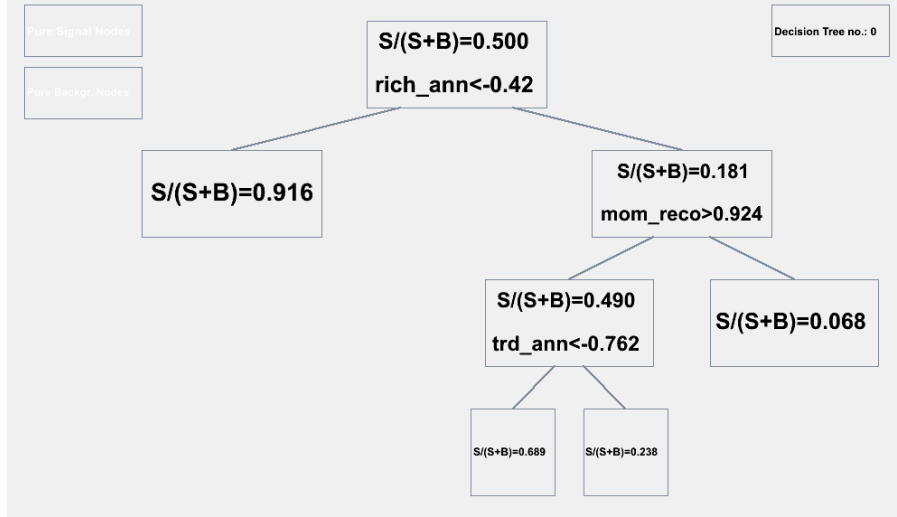


Figure 3.7: The decision tree for the case where RICH, TRD and TOF information is available.

3.9). The TRD detector can help to reject mismatches due to pions while the TOF is more effective to reject kaon and proton tracks (figure 3.10).

The TMVA decision tree offers the highest electron identification efficiency, but also rejects the least amount of mismatches which later contribute to the combinatorial background in the analysis. This leads to a high amount of signal pair efficiency, but also a low signal-to-background ratio for the TVMA cuts. More restrictive cuts on the RICH ANN that reject more mismatches at the loss of true electrons overall performed better in the analysis. The cuts that maximise the significance were used for the dielectron analysis. The cut set with maximum accuracy produced a similar overall performance with a lower signal efficiency but higher signal-to-background ratio (table 3.4). Signal efficiency refers to the amount of signal pairs retained after all cuts divided by number of signal pairs in the acceptance of the CBM detector.

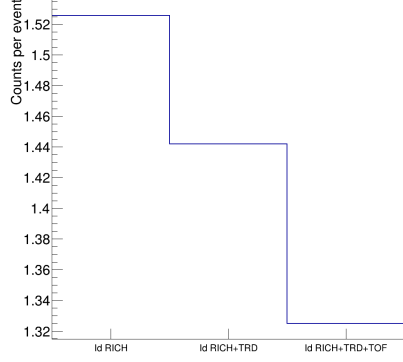
The significance is calculated by

$$\frac{S}{\sqrt{S+B}}. \quad (3.2)$$

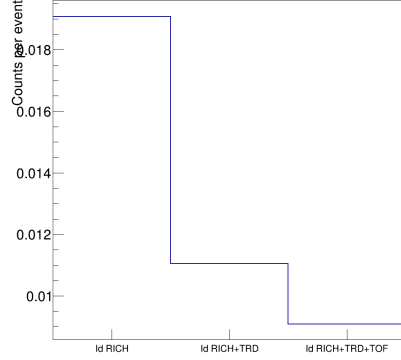
The electron identification efficiency is around 0.8 for Monte-Carlo PID and 0.4 with real PID with all reconstructed electron/positron tracks as denominator (figure 3.11).

Figures 3.12, 3.13 and 3.14 shows the fate of electron and positron emerging from a dilepton decay of a in-medium  $\rho$ ,  $\gamma$ -conversions and  $\pi^0$ -Dalitz decays. The leptons of such a pair are categorized in the following way:

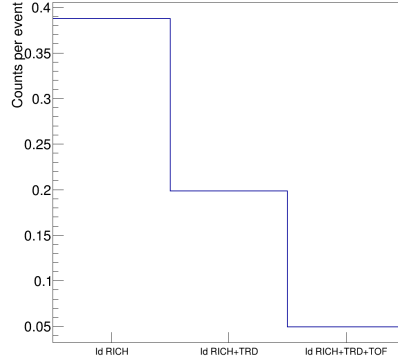
**Identified** The track has a RICH ring, TRD track and TOF hit attached and



(a) Electrons.



(b) Falsely identified Electrons.



(c) Mismatches.

Figure 3.8: Remaining number of electrons and background tracks after each PID step.

PID Cuts	Signal Efficiency	S/B	Significance
Max. Significance	$0.066 \pm 0.004$	$0.076 \pm 0.004$	$4.2 \pm 0.1$
Max. Accuracy	$0.047 \pm 0.003$	$0.11 \pm 0.01$	$4.2 \pm 0.1$
90% Efficiency	$0.064 \pm 0.004$	$0.023 \pm 0.002$	$2.4 \pm 0.1$
80% Efficiency	$0.042 \pm 0.003$	$0.088 \pm 0.007$	$3.6 \pm 0.1$
TMVA	$0.092 \pm 0.005$	$0.031 \pm 0.002$	$3.2 \pm 0.1$

Table 3.4: Results of the dielectron analysis after all analysis cuts are applied. Three Million events were simulated with only the in-medium  $\rho$  embedded. Numbers are for the mass region  $0.55 \text{ GeV}/c^2 \leq m_{inv} \leq 1.2 \text{ GeV}/c^2$ .

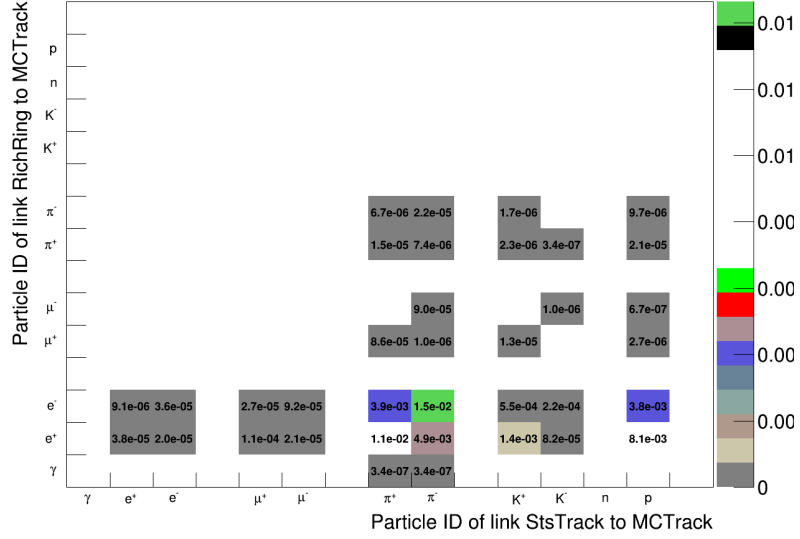


Figure 3.9: This plot shows the Monte-Carlo ID of tracks where the reconstructed track (class StsTrack) and the track associated with the RICH ring are not matched to the same Monte-Carlo track (class MCTrack). Cuts for particle identification in the RICH, TRD and TOF detectors have been applied. Numbers are normalized per event.

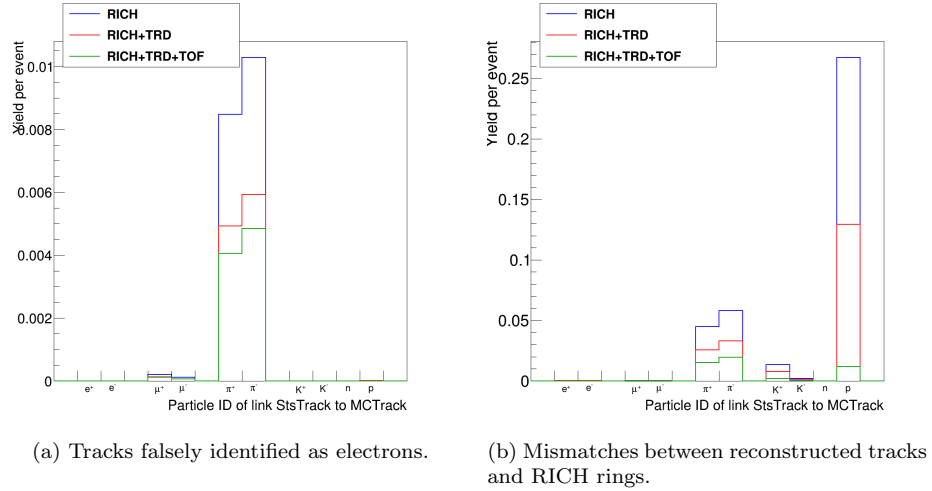


Figure 3.10: Particle type of tracks that were either falsely identified as electrons or mismatches between reconstructed tracks and rings in the RICH.

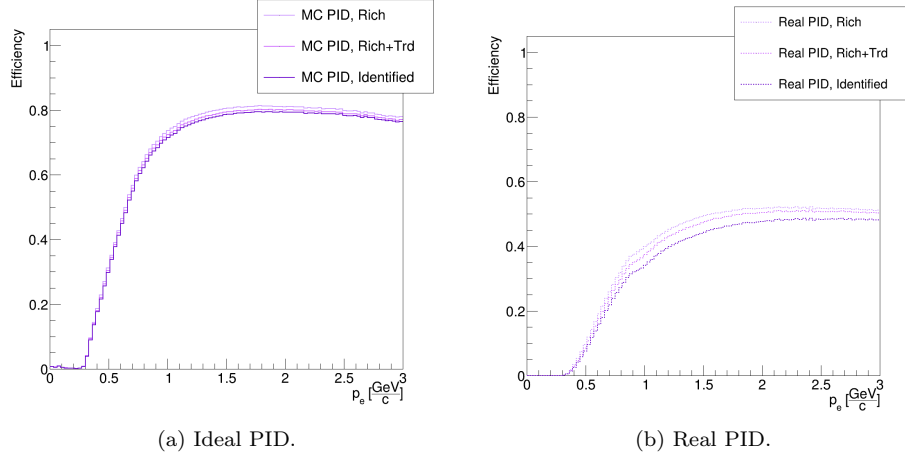


Figure 3.11: Electron identification efficiency for all reconstructed electron tracks when asking for acceptance in the PID detectors only (left) and when using real PID.

has been successfully identified as an electron applying the criteria described earlier.

**PID failed** The track has a RICH ring, TRD track and TOF hit attached, but was not identified as an electron.

**Mismatch** The track reconstructed in the MVD/STS is matched to its corresponding Monte-Carlo track. If this Monte-Carlo track has contributed less than 20% to the RICH ring attached to the reconstructed track then it is considered a mismatch between the track reconstructed in the MVD/STS and the track reconstructed in the PID detectors.

**Accepted PID** The Monte-Carlo track corresponding to the reconstructed track has produced at least 6 Monte-Carlo points in the RICH, 2 in the TRD and 1 in the TOF. Still, the reconstructed track is missing a RICH ring, TRD track or TOF hit attached to it.

**Partially Accepted PID** The Monte-Carlo track corresponding to the reconstructed track has produced Monte-Carlo points in the RICH, TRD or TOF, but not in all three detectors. The track was not correctly identified as an electron/positron.

**Reconstructed** The track was only reconstructed in the MVD and STS.

**Reconstructable** A Monte-Carlo track exists that has produced Monte-Carlo points in at least four different MVD and STS stations, but the track was not reconstructed.

**MC Track** A Monte-Carlo track that has produced at least three points in the MVD or STS. It is in the acceptance of the CBM detector, but did not pass enough MVD and STS stations to be reconstructable.

Each track is only counted once in the highest category that it fits in. To retain a high signal efficiency it is essential that both leptons belonging to the same pair have been identified. As of the cbmroot NOV15 release this is the case for 3% of signal pairs in the acceptance of the CBM detector. Recovering tracks from the “PID failed”, “Mismatch”, “Accepted PID” or “Partially Accepted PID” categories to “Identified” would benefit the dielectron analysis.

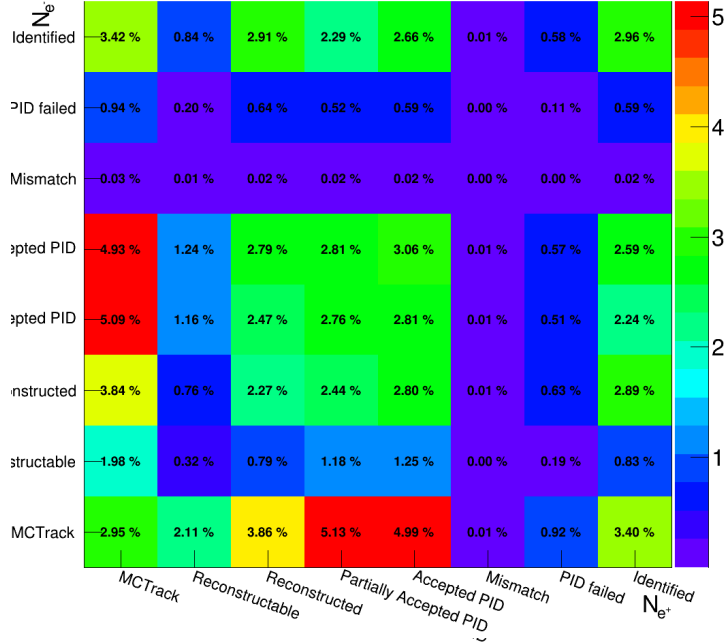


Figure 3.12: Track types of positrons (columns) and electrons (rows) from in-medium  $\rho$  decays that belong to the same pair. The ideal case of a fully identified pair is met by 3% of all tracks in the acceptance. The sum of all pairs adds to 1.

### 3.4 Characteristics of the Background

The main sources of background in the dielectron analysis originate from Dalitz decays of  $\pi^0$ - and  $\eta$ -mesons and photon conversions of direct and decay photons from  $\pi^0 \rightarrow \gamma^* \gamma$  and  $\eta \rightarrow \gamma^* \gamma$  (table 3.5).

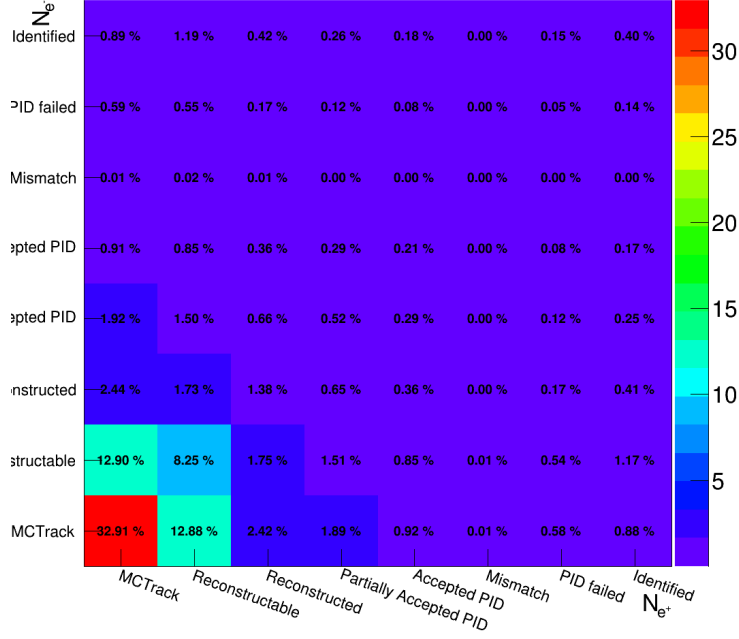


Figure 3.13: Track types of positrons (columns) and electrons (rows) from photon conversion that belong to the same pair. The sum of all pairs adds to 1.

Source	Accepted pairs
$\gamma \rightarrow e^+e^-$	8.2
$\pi^0 \rightarrow \gamma e^+e^-$	0.81
$\eta \rightarrow \gamma e^+e^-$	0.022

Table 3.5: Number of dielectron pairs in the acceptance from different background sources.



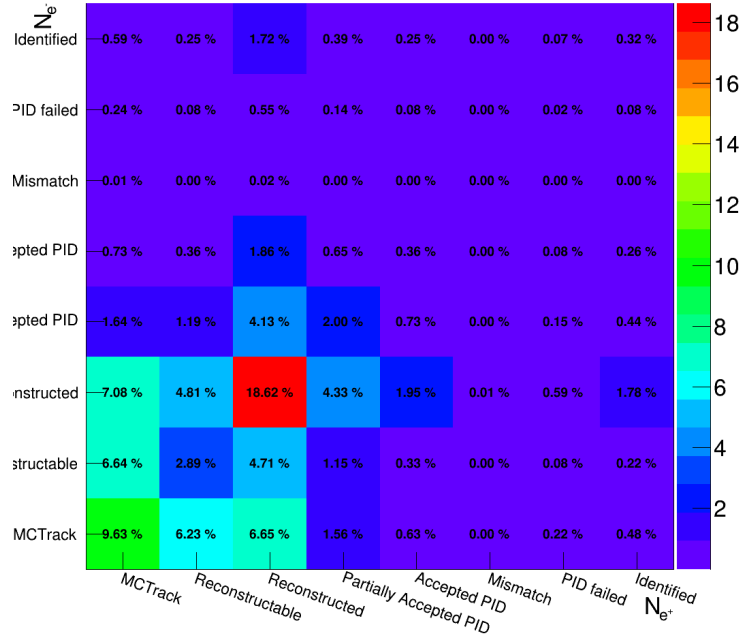


Figure 3.14: Track types of positrons (columns) and electrons (rows) from  $\pi^0$ -Dalitz decays that belong to the same pair. The sum of all pairs adds to 1.

When a photon interacts with a strong electric field like that in the vicinity of a nucleus it can produce a positron/electron pair. In order to conserve both energy and momentum the nucleus will receive some recoil. The photon must carry this recoil energy in addition to the two electron masses  $2m_e \simeq 1.22 \text{ MeV}/c^2$ . Assuming the recoil of the nucleus is small the available kinetic energy for pair production is  $T = h\nu - 2m_e c^2$ .

The main difference between dileptons decays of real photons, virtual photons and Dalitz decays is the opening angle of the pair which depends on its invariant mass:

$$\begin{aligned}
m_{inv}^2 &= (P_{e+} + P_{e-})^2 \\
&= (E_{e+} + E_{e-})^2 - (\vec{p}_{e+} + \vec{p}_{e-})^2 \\
&= E_{e+}^2 - \vec{p}_{e+}^2 + E_{e-}^2 - \vec{p}_{e-}^2 + 2(E_{e+}E_{e-} - \vec{p}_{e+} \cdot \vec{p}_{e-}) \\
&\simeq 2\|\vec{p}_{e+}\| \|\vec{p}_{e-}\| (1 - \cos \Theta) \\
&= 2\langle p_e \rangle \sin^2 \frac{\Theta}{2}.
\end{aligned} \tag{3.3}$$

Real photons do not carry a mass while virtual photons can obtain a mass due to Heisenberg's uncertainty principle. The electrons and positrons from  $\gamma$ -conversions will have a small opening angle and fly in almost the same direction as the photon. A  $\pi^0$ -meson has a larger mass that can contribute to the opening angle of the pair.

Dielectrons from these background sources can be found at small opening angles, invariant masses and lower momenta (figures 3.15 and 3.16).

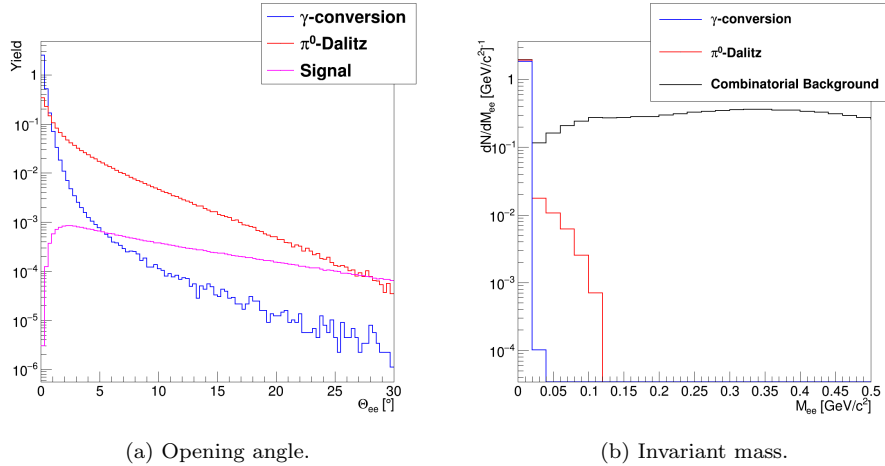


Figure 3.15: Invariant mass of dielectrons from  $\gamma$ -conversion,  $\pi^0$ -Dalitz decays, signal and of the combinatorial background. The signal source is only the in-medium  $\rho$ .

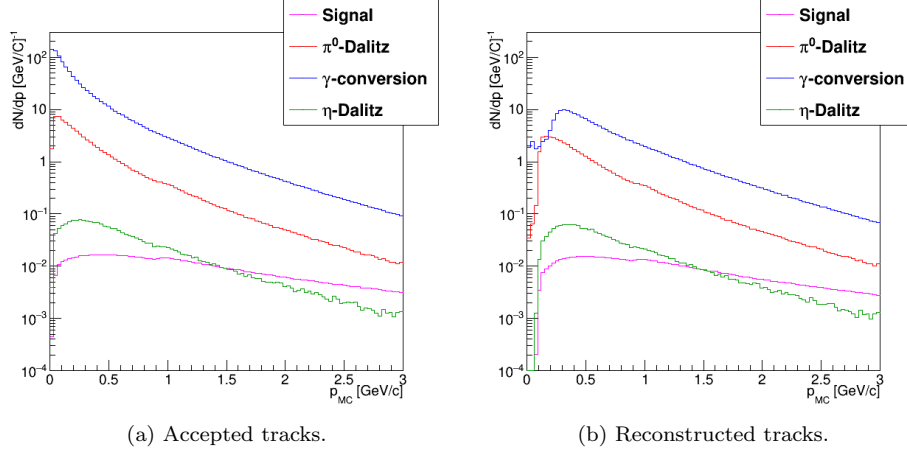


Figure 3.16: Momentum of electrons and positrons from different sources for accepted and reconstructed tracks. For the reconstructed tracks the momentum of the corresponding Monte-Carlo track is plotted. The signal source is the in-medium  $\rho$ .

### 3.5 Possible Role of the MVD

To reject partially identified background pairs a wedge cut is applied taking into account the the opening angle of an identified electron to its closest neighbour without particle identification and product of the momenta of the two tracks (section 3.6.4). This cut will not work if the partner of the identified particle had such a low momentum that it did not pass enough STS stations to be reconstructed. The MVD stations are located closer to the target than the STS. Employing the MVD as tracking stations in addition to the STS results in more reconstructed tracks (figure 3.17) which should make the topology cut more effective. Downsides are the  $\delta$ -electrons that reach the MVD (chapter 3.8.3) and the additional material of the MVD that produces more  $\gamma$ -conversions close to the target (chapter 3.6.3).

Another approach would be to use the distance of the identified electron track to its nearest hit in the first MVD station. If the integrated magnetic field between the target the first MVD station were small enough this would allow to find conversions where one track of the pair was not reconstructed, but only left a hit in the first station (chapter 3.7.1).

The excellent position resolution of the MVD may help to find tracks from  $\gamma$ -conversions that have left hits in the first MVD stations, but were not reconstructed (chapter 3.7.3).

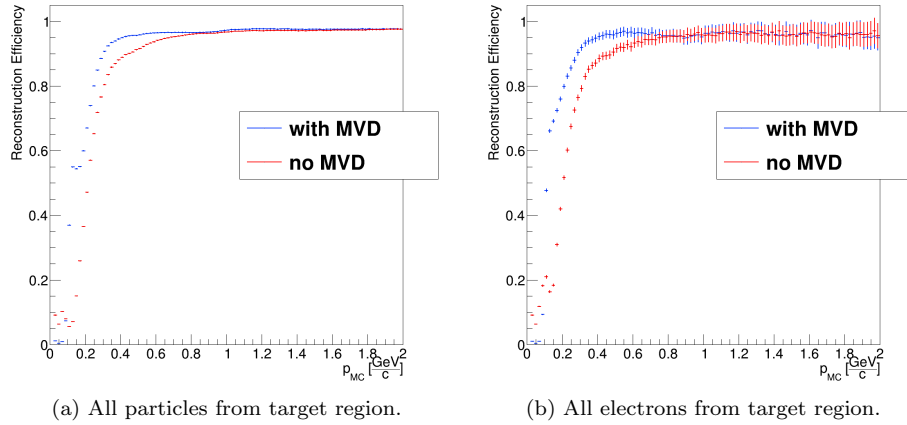


Figure 3.17: The reconstruction efficiency with and without the MVD for tracks from the target region.

## 3.6 Background Rejection

The studies in this section have been done with ideal particle identification.

### 3.6.1 KFParticle

KFParticle is a software package for the reconstruction of secondary vertices and calculation of the parameters of the decayed particle. The Kalman filter method has been modified to work with an extended model of measurements. The algorithm provides the vertex position and an estimate of the track parameters. It is possible to refine the vertex position and track parameters applying additional constraints, for example on the topology and mass. The parameters of the decayed particle are calculated at both the point of production and the point of its decay.

#### KFParticleFinder

The *KFParticleFinder* is a task that runs reconstruction of short-lived particles including  $\gamma$ -conversions. Figure 3.18 shows the z-position of the vertex of all  $\gamma$ -conversions reconstructed with the *KFParticleFinder*. As it is unlikely that both the electron and positron from a  $\gamma$ -conversion reach the PID detectors the reconstruction efficiency is only 5% for primary conversions and 1.5% for conversions outside the target region.

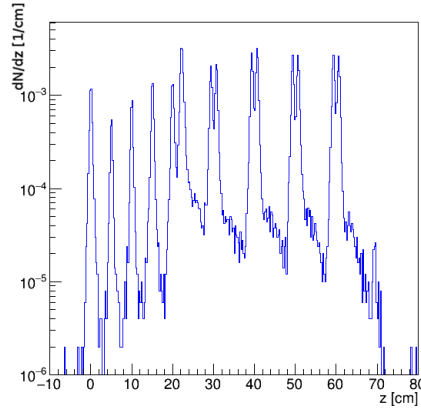


Figure 3.18: The reconstructed  $z$ -vertex of  $\gamma$ -conversions found with the KFParticleFinder per event.

### Custom Analysis with KFParticle

A larger source of the background are partially identified  $\gamma$ -conversions. An identified electron/positron is combined with a reconstructed track without particle identification into a *KFParticle* object. Figure 3.19 shows the results for pairs from photon conversions and random combinations of tracks. A pair is rejected as a  $\gamma$ -conversion if the  $z$ -position of the reconstructed decay vertex is larger than  $4\text{ cm}$ . Due to the large combinatorial background of pairs that fit in the target region are not considered. The  $\chi^2$  of the fit is not suitable to distinguish true and fake pairs. Cuts are applied based on opening angle ( $\theta < 2^\circ$ ) and mass ( $m < 5\text{ MeV}/c^2$ ).

#### 3.6.2 Photon Conversion Cut

Dielectrons from  $\gamma$ -conversions have smaller invariant masses than other sources (3.15). Identified pairs with a mass of less than  $25\text{ MeV}$  are removed from the analysis. This cut is not suitable to reject partially identified pairs.

#### 3.6.3 Primary Vertex Cut

Dielectrons from the decay of  $\rho^0$ ,  $\omega$  and  $\phi$  come from the target while those from  $\gamma$ -conversions can be produced in any detector material as well. To identify tracks that come from outside of the target region a reconstructed track is extrapolated with *CbmL1PFFitter::GetChi2Vertex()* to the  $z$ -position of the reconstructed primary vertex. A cut is then applied based on the lateral deviation

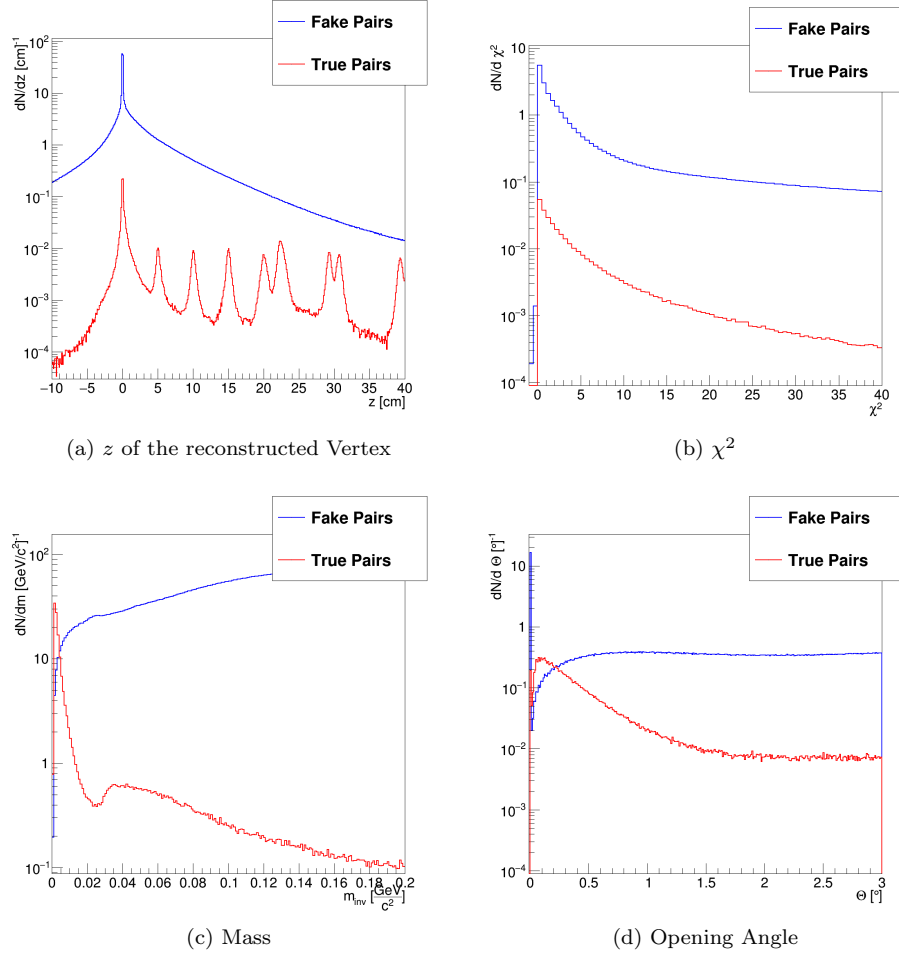


Figure 3.19: The  $z$ -position of the reconstructed vertex,  $\chi^2$  of the fit, reconstructed mass of the mother particle reconstructed with KFParticle and the opening angle between the daughter particles.

of the extrapolated track to the primary vertex:

$$\sqrt{\chi^2} = \sqrt{\frac{1}{2} \cdot \frac{(\Delta x)^2 \cdot C_{yy} - 2 \cdot \Delta x \cdot \Delta y \cdot C_{xy} + (\Delta y)^2 C_{xx}}{C_{xx}C_{yy} - C_{xy}^2}}. \quad (3.4)$$

The deviation takes errors from the covariance matrix  $C$  into account. The results of the extrapolation for electrons from  $\pi^0$ -Dalitz and  $\gamma$ -conversions that come from the the primary vertex and from  $\gamma$ -conversions that are produced outside the target region can be seen in figure 3.20. The cutoff values were chosen such that the significance of the  $\chi$ -distribution is highest which are 2.7 for the setup with the MVD and 3.6 without the MVD.

The separation is better without the MVD in the geometry setup. Figure 3.21 shows the z-position of the location of  $\gamma$ -conversions. With the primary vertex cut electrons from conversions produced in the first three MVD stations can not be identified as effectively as conversions in detector stations further away from the target.

In order to better reject secondary tracks produced in the MVD a new cut was applied that asks for a hit in the first MVD station. If such a hit is not present then the track is extrapolated to the first MVD station and it is removed from the analysis if the predicted hit position is not within the acceptance of the station or the beam hole. A large amount of the tracks coming from the primary vertex are extrapolated in the inner hole of the first MVD station (figure 3.22). Not including the inner hole of the MVD station would lead to a large loss of primary tracks. With this additional cut it is possible to reject more conversions produced in the MVD stations (figure 3.23).

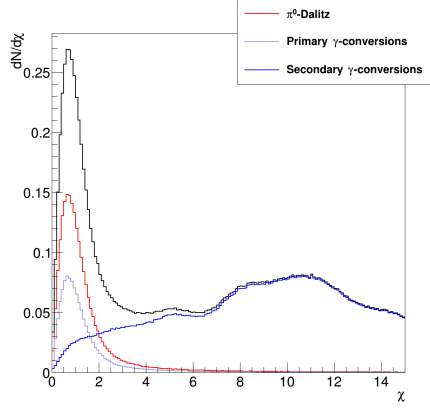
The deviation used for the primary track cut takes track extrapolation errors into account. Therefore, large errors would result in a small  $\chi^2$ . As an alternative the cut is made on the radial distance. Figure 3.24 shows the distance to the primary vertex for different sources.

Figure 3.25 compares the signal-to-background ratio after each analysis step when cutting either with a  $\sqrt{\chi^2}$  value of 2.7 or radial distance of  $140 \mu m$ . Only the in-medium  $\rho$  was embedded into UrQMD events and only acceptance of a track in the RICH and TRD detectors was required for particle identification. The primary vertex cut alone is more effective when cutting with the radial distance. The cut on  $\sqrt{\chi^2}$  benefits when combined with the requirement that the track must be in the acceptance of the first MVD station.

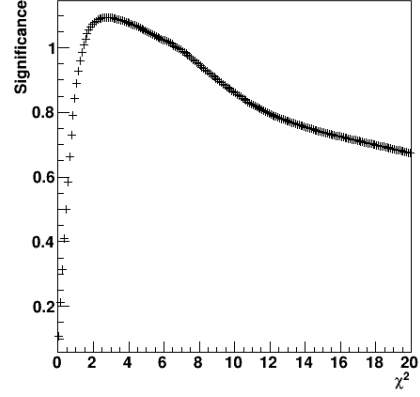
As can be seen in table 3.6 using the  $\sqrt{\chi^2}$  as cutoff value retains more signal pairs while the signal-to-background ratio is the same. Since cutting on the radial distance offers no benefit to the analysis the  $\sqrt{\chi^2}$  has been used.

### 3.6.4 Track Topology Cut

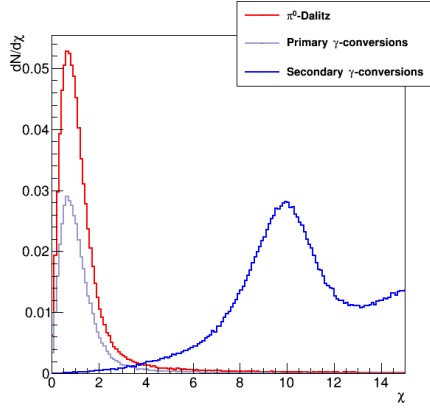
This cut aims to find partially identified pairs. For each electron with particle identification and its closest reconstructed track that has no PID a triangular cut is applied based on the product of the momenta and the opening angle  $\Theta_{e^\pm}$  of these two tracks:  $\sqrt{p_{e^\pm} \cdot p_{rec}} \leq 1.8 \text{ GeV}/c$  and  $\Theta_{e^\pm, rec} \leq 2.2^\circ$ . The distribution



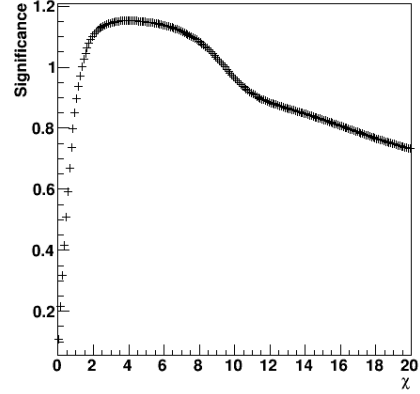
(a) Quality of primary vertex fit with the MVD.



(b) Significance of cutoff points with the MVD.



(c) Quality of primary vertex fit without the MVD.



(d) Significance of cutoff points without the MVD.

Figure 3.20: Quality of the fit to the primary vertex with the MVD (upper row) and without the MVD (lower row). The cutoff values to separate electrons from  $\pi^0$ -Dalitz and  $\gamma$ -conversions that come from the primary vertex and those that are produced outside the target region were chosen based on the significance of the  $\chi$ -distribution.



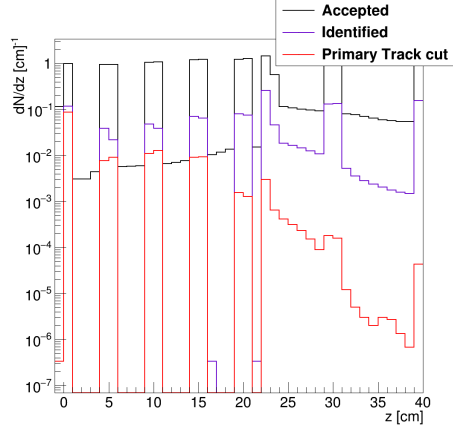


Figure 3.21: The  $z$ -position of the start vertex of all  $\gamma$ -conversions in the acceptance and that remain after particle identification and the primary track cut.

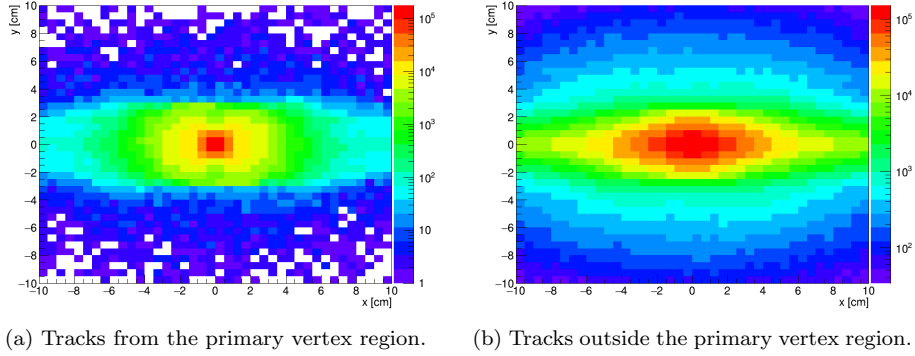


Figure 3.22: The estimated  $x$ - and  $y$ -Position of tracks extrapolated to the first MVD station. A large portion of tracks from the primary vertex region pass the MVD through its inner hole at  $|x| \leq 5 \text{ mm}$  and  $|y| \leq 5 \text{ mm}$ .

Cut	Signal Efficiency	S/B	Significance
$\sqrt{\chi^2}$	$0.28 \pm 0.01$	$0.25 \pm 0.01$	$14.7 \pm 0.1$
Radial Distance	$0.25 \pm 0.01$	$0.26 \pm 0.01$	$14.1 \pm 0.1$

Table 3.6: Results of the dielectron analysis when using the  $\sqrt{\chi^2}$  or radial distance value as cut value for the primary vertex cut for the mass range of  $0.55 \text{ GeV}/c^2$  to  $1.2 \text{ GeV}/c^2$ .

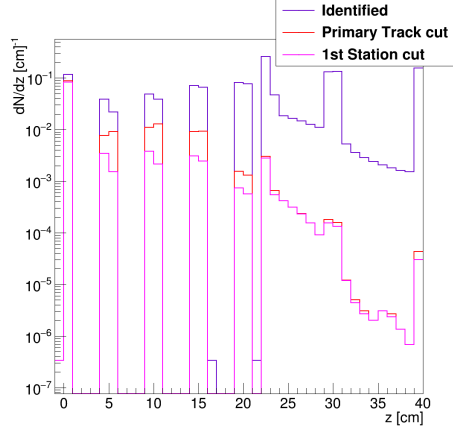


Figure 3.23: The  $z$ -position of the start vertex of all  $\gamma$ -conversions that remain after particle identification, the primary track cut and after extrapolation to the first MVD station.

for background tracks makes a separation less effective without the MVD in the setup (figure 3.26). The cutoff values were chosen such that the significance is highest (figure 3.27).

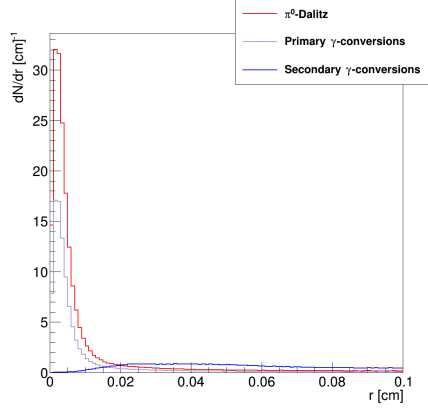
## 3.7 Failed Strategies for Background Rejection

### 3.7.1 Hit Topology Cut

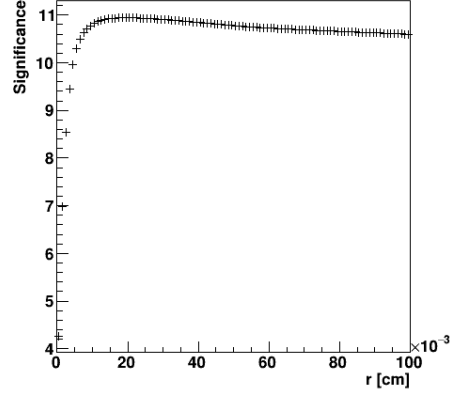
A cut that uses the momentum of the identified particle and the distance to the nearest hit in the first MVD station that was not used by a reconstructed track has been successfully applied in [20]. The cut has been compared for different magnetic field strengths. There is no longer a correlation between these two observables (figures 3.28 and 3.29). The field configuration has been changed considerably since 2009 and the field integral is no longer small enough to take advantage of this feature.

### 3.7.2 Transverse Momentum Cut

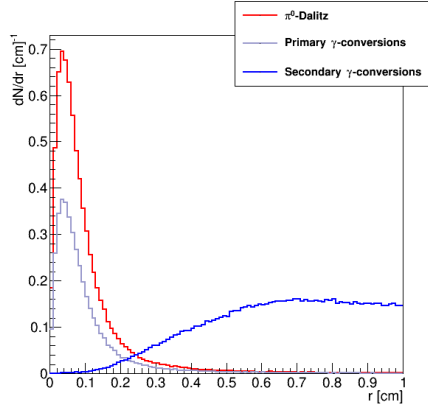
Due to the small decay momentum and the strong fall-off of the centre of mass momentum, lepton tracks from background sources can typically be found at low transverse momenta. Such a cut would exclude part of the phase space and remove contributions to the signal invariant mass spectrum from Dalitz decays of  $\pi^0$ ,  $\eta$  and  $\omega$ . Since the transverse momentum of tracks that survive the track topology is no longer a good separation criterium (figure 3.30) this is no longer an issue.



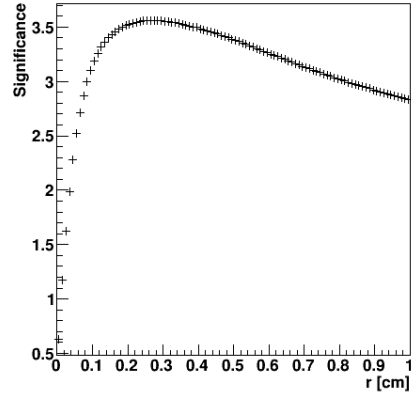
(a) Radial distance of tracks to the primary vertex with the MVD in the setup.



(b) Significance of cutoff points with the MVD in the setup.



(c) Radial distance of tracks to the primary vertex without the MVD in the setup.



(d) Significance of cutoff points without the MVD in the setup.

Figure 3.24: Tracks are extrapolated to the primary vertex. Shown is the radial distance to the primary vertex with the MVD (upper row) and without the MVD (lower row) in the setup. The cutoff values to separate electrons that come from the primary vertex and those that are produced outside the target region were chosen based on the significance.

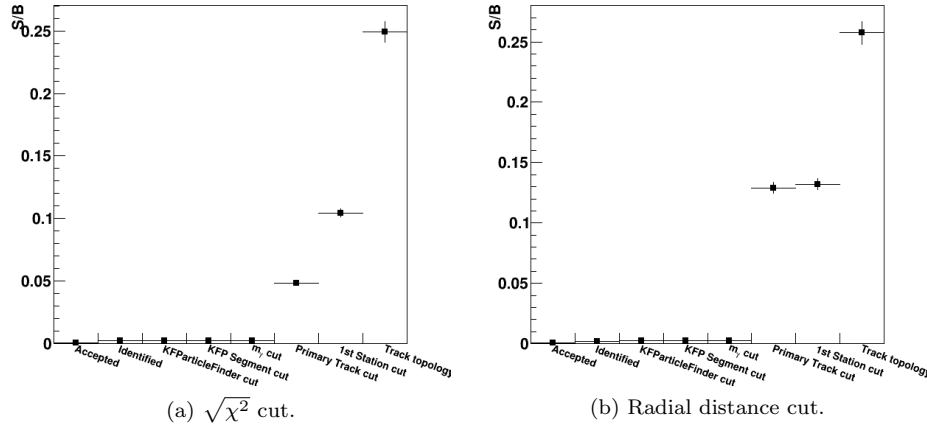


Figure 3.25: Signal-to-background in the mass range of  $0.55 \text{ GeV}/c^2 - 1.2 \text{ GeV}/c^2$  when applying the primary vertex cut using either the  $\sqrt{\chi^2}$  or radial distance value.

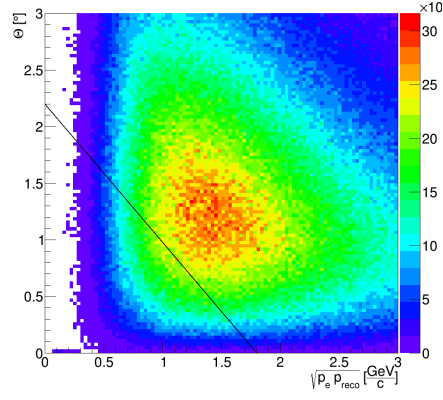
### 3.7.3 Photon Vertex Reconstruction in the MVD

This approach assumes that one partner of the conversion has been identified as an  $e^+/e^-$  while the decay partner could not be reconstructed, but has produced enough hits in the MVD to find this track. Constraints for the initial position and momentum of this track are that dielectrons from conversion come from a common vertex, have a small opening angle and small invariant mass.

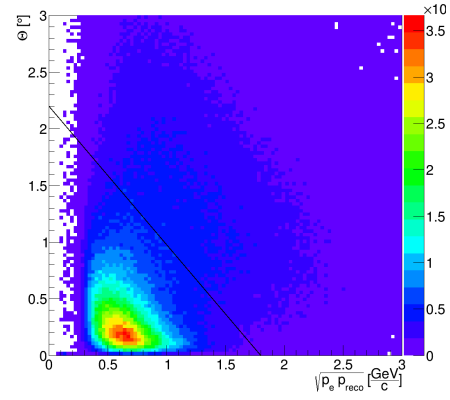
To realize this a track finder is needed. LitTrack is a software library of cbmroot intended to extend tracks reconstructed in the STS to the RICH, TRD and TOF detectors. The source files are well documented and the software is structured. The package includes classes for track propagation, track finding and fitting. Many of them are written in a generic way allowing for flexible use.

LitTrack realizes track finding by employing a method commonly known as track following. It needs a track seed, i.e. a position and momentum vector, as input. The track is then extrapolated to the next detector layer. Different techniques are available to associate detector hits with a track. Only the closest hit within the validation gate can be attached (nearest neighbour). Alternatively, a branch is created for every hit within the validation gate. The track state is updated with the Kalman filter method. This process is then repeated for all detector layers.

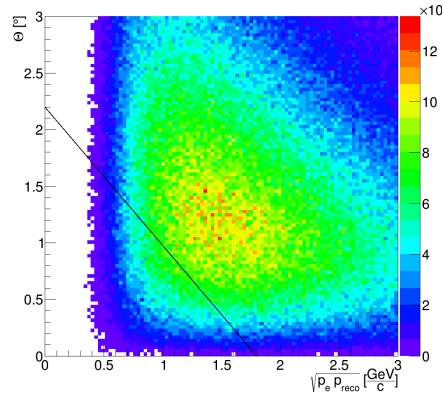
To test that LitTrack was set up correctly only Monte-Carlo information was used. The tracks were positrons and electrons with at least three points in the MVD and momentum of at least  $50 \text{ MeV}/c$ . Initial position and momentum were taken from the start vertex of the Monte-Carlo track. All Monte-Carlo points from the MVD and STS were included in the search space. After finishing with



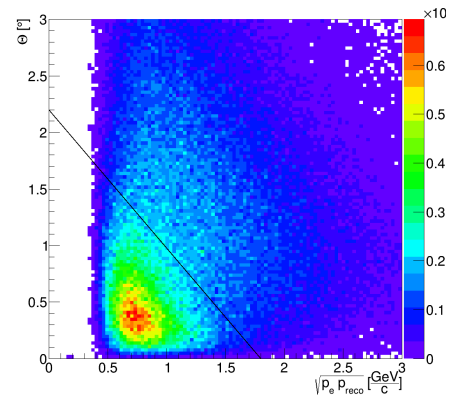
(a) Topology of signal tracks with the MVD in the setup.



(b) Topology of background tracks with the MVD in the setup.



(c) Topology of signal tracks without the MVD in the setup.



(d) Topology of background tracks without the MVD in the setup.

Figure 3.26: Comparison of the track topology for signal (in-medium  $\rho$ ) and background tracks.

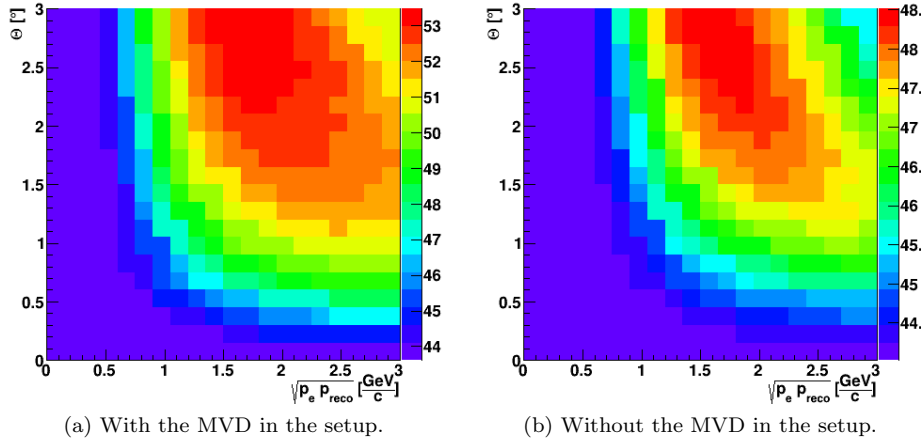


Figure 3.27: Significance for different cut values of the track topology cut.

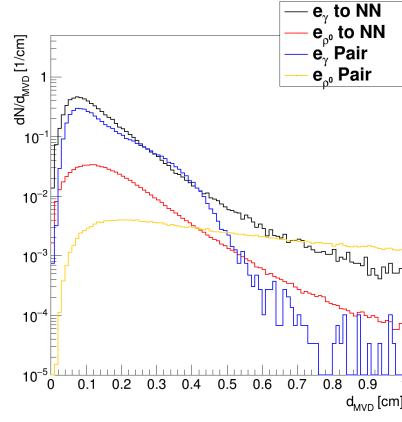
the search LitTrack returns a list of tracks. A track is considered as found if at least 60% of the attached points belong to the true Monte-Carlo track. A track that consists of 3 points would still count as found if two points were correctly attached. As can be seen in figure 3.31 most of the tracks could be found. The efficiency drops for low momenta as a lot of the tracks start curling and produce multiple hits in the same detector layer.

In the next step reconstructed data was used. Hits in the MVD and STS that have already been assigned to a reconstructed track were excluded from the track search. Some assumptions were made to test the feasibility of such an approach: Candidates for the search are conversions where one decay particle has been reconstructed and has a RICH ring attached to it. The decay partner was not reconstructed, but the corresponding Monte Carlo track produced at least three hits in different MVD or STS stations. In around 30% of all cases where the unreconstructed decay partner produced at least one hit in the MVD or STS, there are at least three in different stations making it a possible candidate for this track finding approach. Most of the candidates have momenta of around 100 MeV/c (figure 3.32).

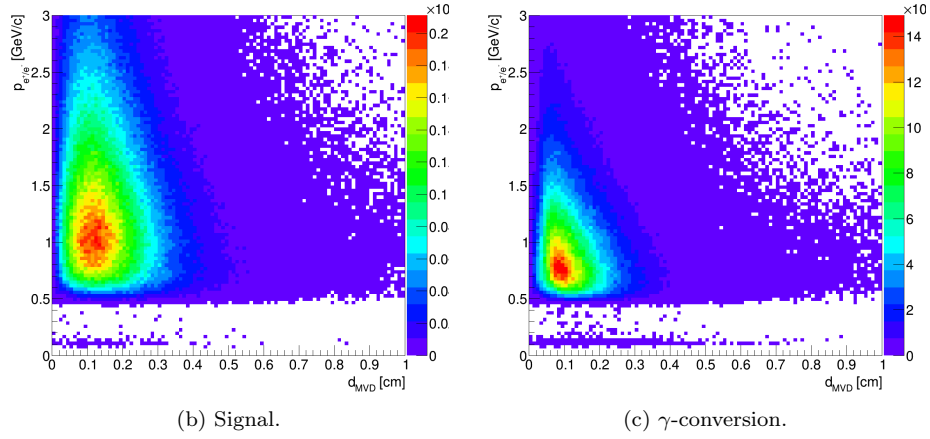
The reconstructed track is extrapolated to their Monte Carlo decay vertex. The position and direction of the extrapolated track serve as track seed for the track finder. Invariant mass and opening angle of the conversion pairs are shown in figure 3.33. The momentum was estimated with the formula

$$p = \frac{m_{inv}^2}{4 \sin^2(\Theta/2) \cdot p_{id}} \quad (3.5)$$

with  $m_{inv} = 0.0006 \text{ GeV}/c^2$ ,  $\Theta = 0.1^\circ$  and  $p_{id}$  is the momentum of the track with particle identification.



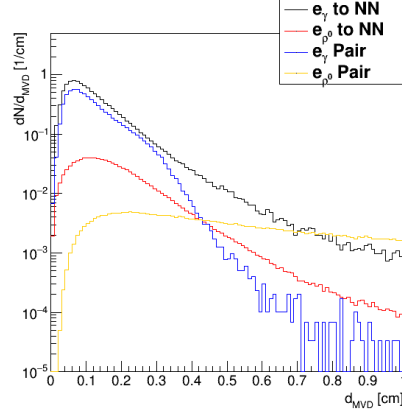
(a) Distance to closest hit on the first MVD station.



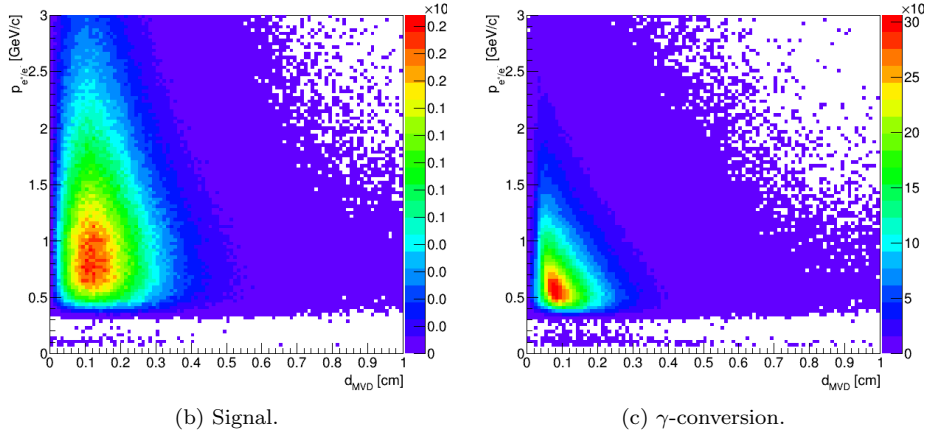
(b) Signal.

(c)  $\gamma$ -conversion.

Figure 3.28: Top row: the distance of a hit from a  $\gamma$ -conversion and signal (in-medium  $\rho$ ) to the nearest hit that does not belong to a reconstructed track. Also plotted is the distance of the true partners in the first MVD station. Bottom row: Momentum of the identified electron vs. distance to the nearest hit on the first MVD station for signal and  $\gamma$ -conversion decays. Full field is applied.



(a) Distance to closest hit on the first MVD station.



(b) Signal.

(c)  $\gamma$ -conversion.

Figure 3.29: Top row: the distance of a hit from a  $\gamma$ -conversion and signal (in-medium  $\rho$ ) to the nearest hit that does not belong to a reconstructed track. Also plotted is the distance of the true partners in the first MVD station. Bottom row: Momentum of the identified electron vs. distance to the nearest hit on the first MVD station for signal and  $\gamma$ -conversion decays. The field has been reduced to 70%.



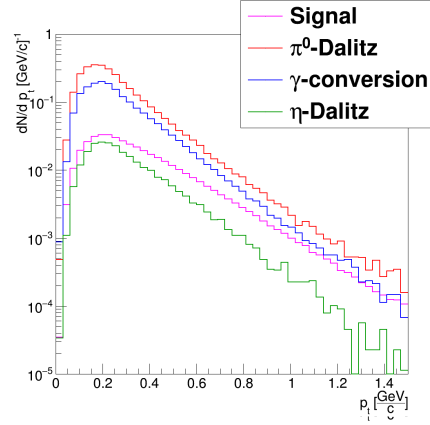


Figure 3.30: Transverse momentum distribution for different sources. Only tracks remaining after the track topology cut are shown.

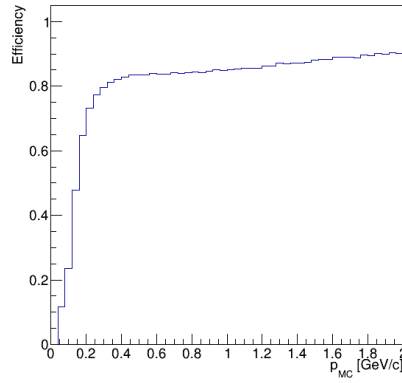


Figure 3.31: Candidate finding efficiency of LitTrack for electron tracks that have at least three points in the MVD. Ideal seeds from the Monte Carlo track were used. Curling tracks are included.

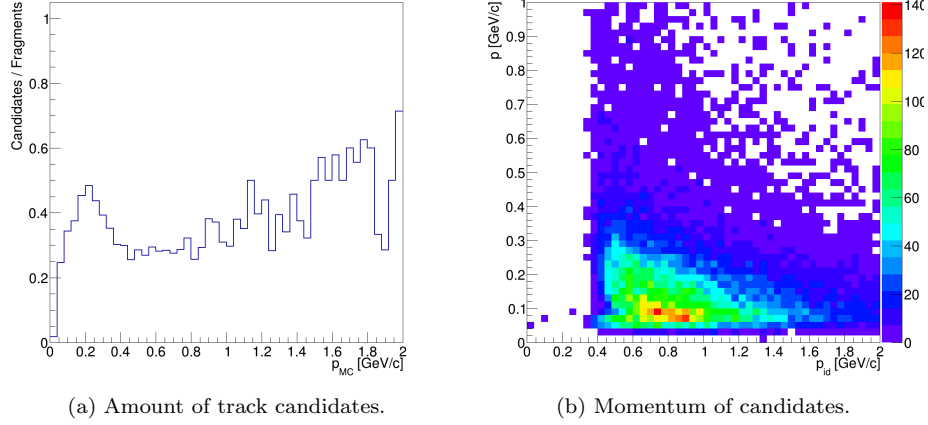


Figure 3.32: Left: Amount of search candidates divided by fragments. Both terms refer to  $e^+/e^-$  pairs from conversions where one particle was reconstructed and has a rich ring attached to it. The decay partner is called a fragment if it was not reconstructed, but the corresponding Monte Carlo track produced at least one hit in the MVD or STS. It is called a candidate if it has produced at least three hits in different MVD or STS stations. Right: The momentum of the track candidate to find versus the momentum of its identified track.

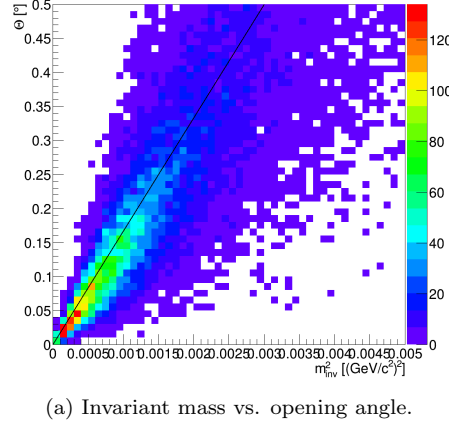


Figure 3.33: Invariant mass versus opening angle of the input pairs for LitTrack.

Because of the small opening angle of conversion pairs extrapolating the identified track to the true start vertex of the conversion the initial position and direction of the seed parameters are almost ideal. However, there is a large uncertainty in the initial momentum (figure 3.34).

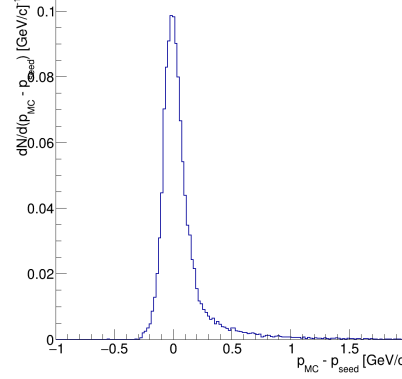


Figure 3.34: Momentum error of the track seed.

The efficiency to find the partner track of the conversion is only around 15% (figure 3.35). A track is considered found if at least 60% of the attached hits can be matched to Monte Carlo points belonging to the correct track. For around 25% of found tracks most or all of the attached hits belong to a different track and for 60% of all candidates no hits had been attached at all.

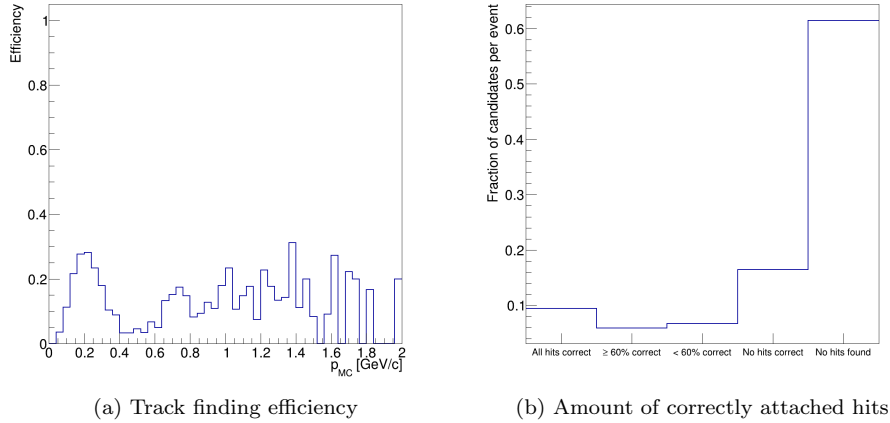


Figure 3.35: Left: Track finding efficiency versus momentum. Right: Amount of tracks where the correct hits, wrong hits or no hits have been attached.

The analysis was repeated smearing the true momentum by 10% and using this value for the track seed. A more accurate initial momentum would increase the performance (figure 3.36).

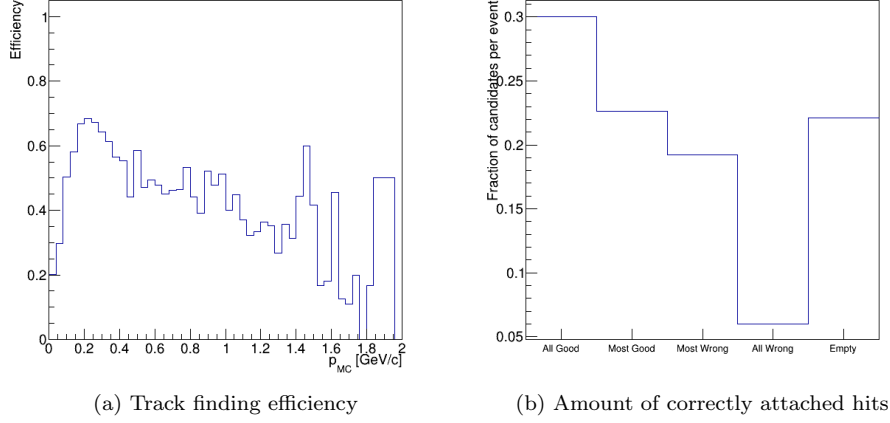


Figure 3.36: Left: Track finding efficiency versus momentum. Right: Amount of tracks where the correct hits, wrong hits or no hits have been attached. The Monte Carlo momentum was smeared by 10% and used as the initial momentum guess for the track finder.

The momentum below 100 MeV/ $c$  of the candidates and the large uncertainty for the momentum of the track seed make this approach unfeasible.

### 3.8 Results of the Analysis

The performance of the dielectron analysis has been compared with and without the MVD in the geometry setup. The  $e^+e^-$  pairs that come from the same source are the signal pairs. Those that originate from different sources form the combinatorial background. The invariant mass spectrum can be divided into five regions where different dielectron decays dominate:

- $0 \text{ GeV}/c^2 \leq m_{inv} \leq 0.15 \text{ GeV}/c^2$ : The low masses are dominated by  $\pi^0$ -Dalitz decays and  $\gamma$ -conversions.
- $0.15 \text{ GeV}/c^2 \leq m_{inv} \leq 0.55 \text{ GeV}/c^2$ : An enhancement of dielectrons due to medium contributions are expected here. The  $\omega$ - and  $\eta$ -Dalitz decays can be found in this region as well.
- $0.55 \text{ GeV}/c^2 \leq m_{inv} \leq 1.2 \text{ GeV}/c^2$ : This is the low mass vector meson region where the  $\omega$ ,  $\phi$  and  $\rho$  mass peaks are located.
- The regions five times the width around the pole masses of the  $\omega$  and  $\phi$ .

Mass Range	Signal Efficiency	S/B	Significance
Setup with the MVD			
$0.0 - 0.15 \text{ GeV}/c$	$(4.7 \pm 0.1) \cdot 10^{-4}$	$5.7 \pm 0.1$	$232 \pm 1$
$0.15 - 0.55 \text{ GeV}/c$	$0.12 \pm 0.01$	$0.27 \pm 0.01$	$64 \pm 1$
$0.55 - 1.2 \text{ GeV}/c$	$0.27 \pm 0.01$	$0.45 \pm 0.01$	$52 \pm 1$
$\omega$	$0.27 \pm 0.01$	$1.2 \pm 0.1$	$44 \pm 1$
$\phi$	$0.32 \pm 0.05$	$0.36 \pm 0.05$	$7.1 \pm 0.5$
Setup without the MVD			
$0.0 - 0.15 \text{ GeV}/c$	$(5.2 \pm 0.1) \cdot 10^{-4}$	$4.7 \pm 0.1$	$266 \pm 1$
$0.15 - 0.55 \text{ GeV}/c$	$0.15 \pm 0.01$	$0.20 \pm 0.1$	$57 \pm 1$
$0.55 - 1.2 \text{ GeV}/c$	$0.33 \pm 0.01$	$0.27 \pm 0.01$	$46 \pm 1$
$\omega$	$0.34 \pm 0.01$	$0.72 \pm 0.01$	$41 \pm 1$
$\phi$	$0.42 \pm 0.06$	$0.19 \pm 0.03$	$6.0 \pm 0.1$

Table 3.7: Comparison of setups with and without the MVD included. Ideal PID has been used.

The signal efficiencies, signal-to-background ratios and significances are given separately for these mass ranges.

### 3.8.1 Ideal PID

As a first step an ideal particle identification is used. Candidates are electron and positron Monte Carlo tracks that have a reconstructed track associated with it and are accepted by the PID detectors. A track is considered to be accepted by the PID detectors if it have at least six Monte Carlo points in the RICH, two in the TRD and one in the TOF detector.

Figure 3.37 shows the invariant mass spectrum before and after all cuts are applied in the analysis. Under these ideal conditions the peak of the  $\omega$ -meson is higher than the background.

The cuts that mainly contribute to reducing the background are the primary vertex cut, the cut that asks for acceptance in the first MVD station and the track topology cut. The effects of the other cuts are negligible (figure 3.38). In the intermediate mass region of  $0.15 \text{ GeV}/c^2$  to  $0.55 \text{ GeV}/c^2$  the signal-to-background ratio drops sharply after the primary vertex cut due to unrealistically high masses of some  $\gamma$ -conversions and  $\pi^0$ -Dalitz decays. The primary vertex cut removes most of these pairs from the analysis. Since this behaviour can not be observed when calculating the invariant mass with the Monte Carlo momentum this is caused by uncertainties in the reconstructed momentum (figure 3.39).

Figure 3.40 and table 3.7 show a comparison of the analysis performance with and without the MVD. The signal-to-background ratio can be improved with the MVD while the signal efficiency drops by around 15%. The significance still shows an overall gain when including the MVD.

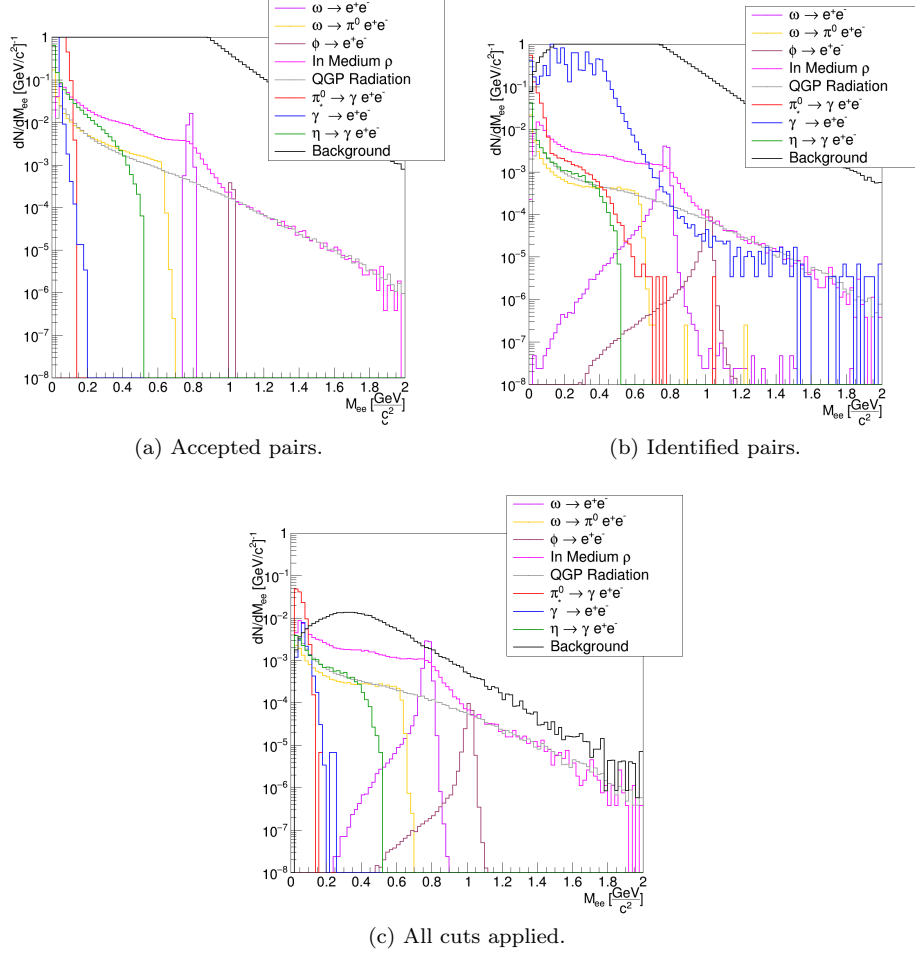


Figure 3.37: The invariant mass spectrum with the combinatorial background and contributions from different sources. Ideal PID has been used.

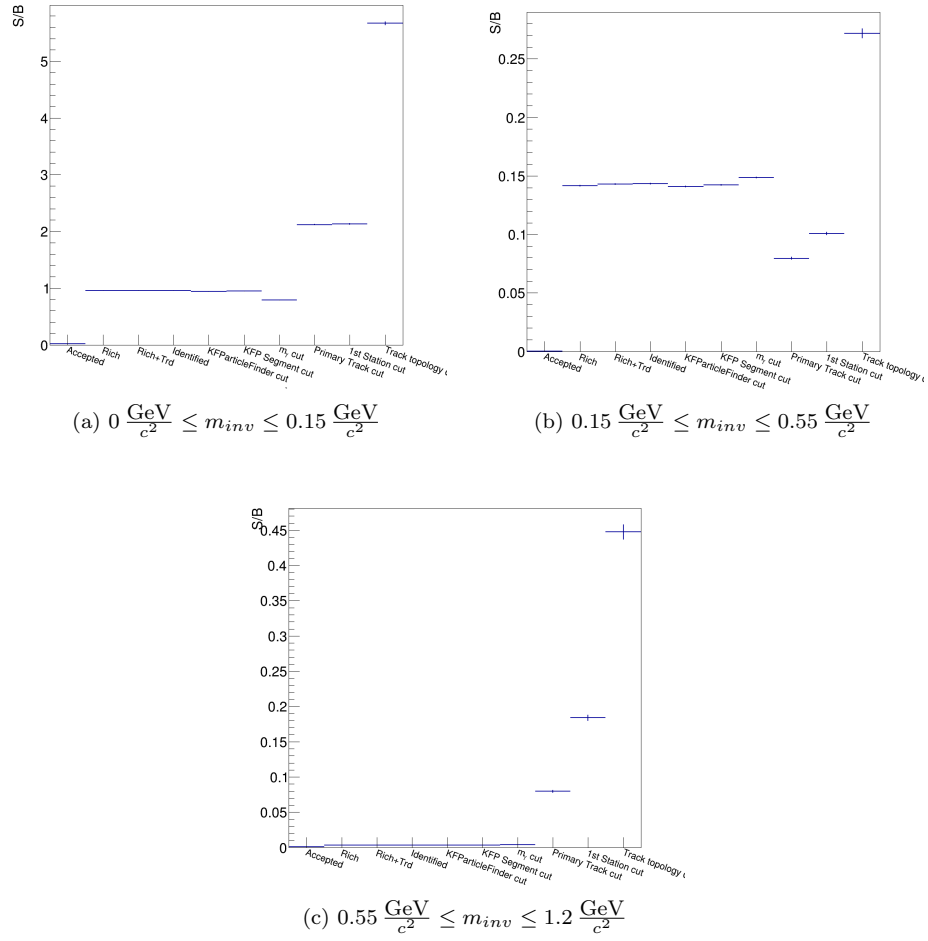
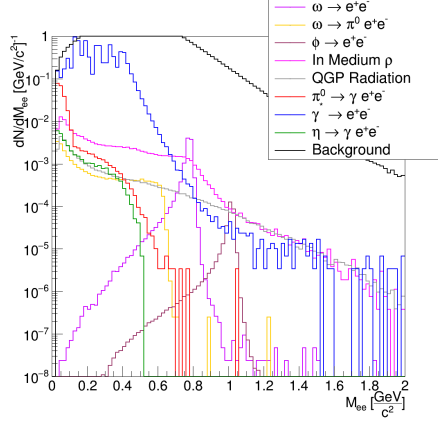
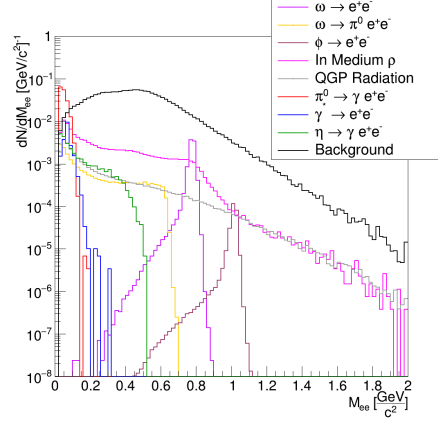


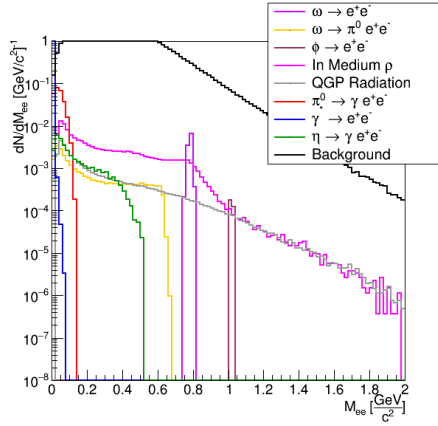
Figure 3.38: The signal-to-background ratio after each cut step. The MVD is included in the setup. Ideal PID has been used.



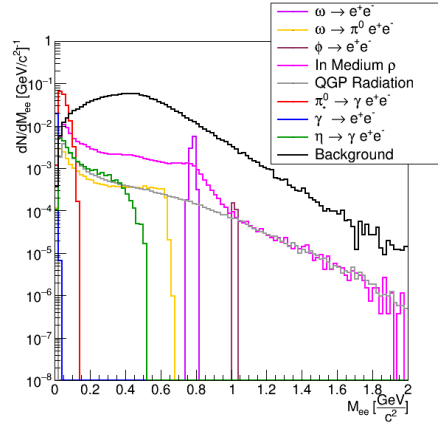
(a) Before the primary vertex cut. Reconstructed momentum.



(b) After the primary vertex cut. Reconstructed momentum.



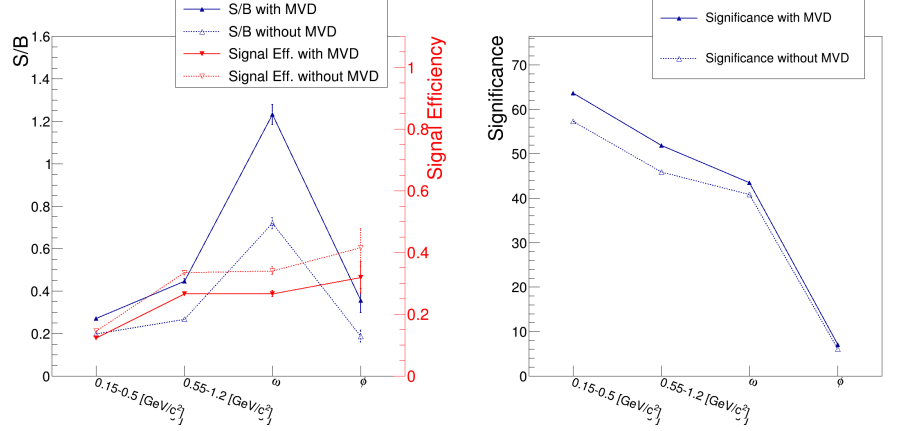
(c) Before the primary vertex cut. Monte Carlo momentum.



(d) After the primary vertex cut. Monte Carlo momentum.

Figure 3.39: The invariant mass spectrum before and after the primary vertex cut. The invariant mass has been calculated with the reconstructed momentum in the upper row and with the Monte Carlo momentum in the lower row. Ideal PID has been used.





(a) Signal-to-background ratio and signal efficiency with and without the MVD (b) Significance with and without the MVD

Figure 3.40: Comparison of signal-to-background, signal efficiency and significance with and without the MVD in the setup for ideal particle ID.

### 3.8.2 Realistic PID

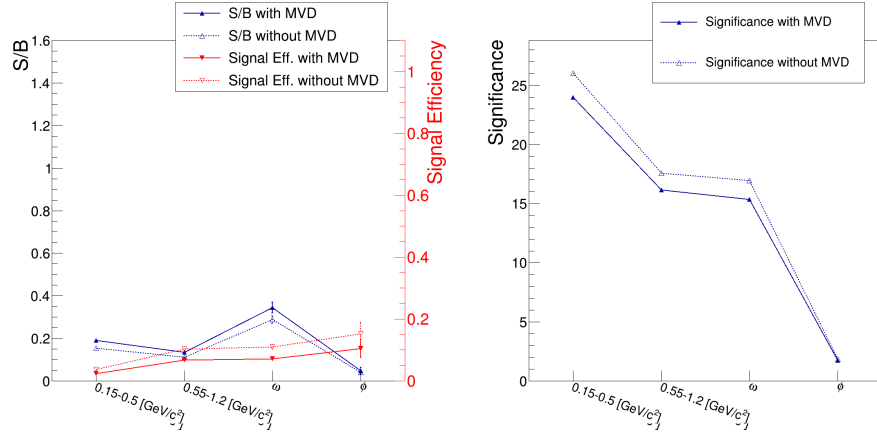
With a realistic particle identification the signal-to-background and signal efficiency are lower than with the ideal PID as would be expected. There is still a gain in the signal-to-background ratio and a loss in signal efficiency when including the MVD in the setup. However, unlike in the case of an ideal PID the overall significance is now better without the MVD than with it (figure 3.41 and table 3.8).

The setup with the MVD starts with a 35% higher combinatorial background due to partially identified pairs from  $\gamma$ -conversions that are produced by the additional material of the MVD while gaining only 10% of fully identified true pairs (table 3.9).

Figure 3.42 shows the detection efficiency of dielectrons from the Pluto cocktail, that means  $\omega$ ,  $\omega$ -Dalitz,  $\phi$  and in-medium  $\rho$ . The detection efficiency is the number of pairs that remain after all analysis cuts are applied divided by the number of pairs generated by Pluto. It is around 11% for ideal PID and 2% for realistic PID.

### 3.8.3 Delta Electrons

Due to its close proximity to the target  $\delta$ -electrons may reach the MVD and produce additional hits. In simulation this is handled by the MVD digitizer *CbmMvdDigitizer::SetDeltaEvents()*. A separate file with  $\delta$ -electron events is generated and random events are then drawn from this file to produce the hits in the MVD.



(a) Signal-to-background ratio and signal efficiency with and without the MVD (b) Significance with and without the MVD

Figure 3.41: Comparison of signal-to-background, signal efficiency and significance with and without the MVD in the setup for realistic particle ID.

Mass Range	Signal Efficiency	S/B	Significance
Setup with the MVD			
$0.0 - 0.15 \text{ GeV}/c$	$(9.8 \pm 0.1) \cdot 10^{-5}$	$4.3 \pm 0.1$	$103 \pm 1$
$0.15 - 0.6 \text{ GeV}/c$	$0.023 \pm 0.001$	$0.19 \pm 0.01$	$24.0 \pm 0.1$
$0.6 - 1.2 \text{ GeV}/c$	$0.067 \pm 0.003$	$0.14 \pm 0.01$	$16.2 \pm 0.1$
$\omega$	$0.072 \pm 0.005$	$0.34 \pm 0.03$	$15.4 \pm 0.1$
$\phi$	$0.11 \pm 0.03$	$0.049 \pm 0.013$	$1.7 \pm 0.1$
Setup without the MVD			
$0.0 - 0.15 \text{ GeV}/c$	$(1.6 \pm 0.1) \cdot 10^{-4}$	$3.7 \pm 0.1$	$122 \pm 1$
$0.15 - 0.6 \text{ GeV}/c$	$0.037 \pm 0.001$	$0.15 \pm 0.01$	$26.0 \pm 0.1$
$0.6 - 1.2 \text{ GeV}/c$	$0.10 \pm 0.01$	$0.11 \pm 0.01$	$17.6 \pm 0.1$
$\omega$	$0.11 \pm 0.01$	$0.29 \pm 0.02$	$16.9 \pm 0.1$
$\phi$	$0.15 \pm 0.04$	$0.041 \pm 0.010$	$1.8 \pm 0.1$

Table 3.8: Comparison of setups with and without the MVD included. Realistic PID has been used.

Setup	Partially Identified Pairs	Fully Identified Pairs
After Particle Identification		
Ideal PID with MVD	1.848	0.203
Ideal PID without MVD	1.525	0.177
Real PID with MVD	0.859	0.0557
Real PID without MVD	0.731	0.0499
After All Cuts		
Ideal PID with MVD	0.123	0.0104
Ideal PID without MVD	0.139	0.00984
Real PID with MVD	0.0545	0.00165
Real PID without MVD	0.0689	0.00173

Table 3.9: Number of partially and fully identified pairs after particle identification for different PID methods and detector setups.

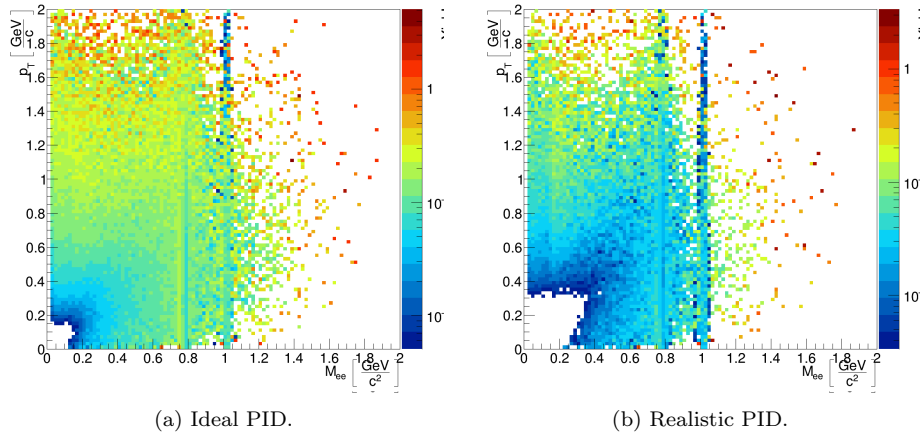


Figure 3.42: The detection efficiency of dielectrons from the low mass vector mesons sources with ideal and realistic particle identification.

The number of beam ions producing  $\delta$ -electrons is equal to the interaction rate, i.e. the number of nuclear collisions per second, divided by the probability for a nuclear collision. For a target with 1% interaction probability this would mean that for each nuclear collision 100 Au ions cross the target and produce, on average,  $\delta$ -electrons. The readout time for an MVD frame is  $10\mu s$  for ASTRAL chips. Taking an interaction rate of  $100 kHz$  which corresponds to 1 event per readout frame the number of ions passing through a 1% target would be

$$N_{ion} = \frac{10^4}{10^{-2}} \frac{ions}{s} \cdot 10^{-5} \frac{s}{frame} = 10 \frac{ions}{frame}. \quad (3.6)$$

The number of  $\delta$ -electrons produced per incident ion is:

$$\frac{dN}{dT} = a \frac{1}{T} \left( 1 - \frac{T}{T_{max}} \right) \quad (3.7)$$

where  $a = 207 \text{ MeV}$  for a 1% target,  $T$  is the kinetic energy of the  $\delta$ -electron and  $T_{max}$  the maximum kinetic energy which can be imparted to a free electron in a single collision

$$T_{max} = 2m_e c^2 \beta^2 \gamma^2 \quad (3.8)$$

which is 73 MeV for an 8A GeV gold projectile. Integrating 3.7 yields

$$N = a \cdot \left( \frac{1}{T_{min}} - \frac{1}{T_{max}} + \frac{1}{T_{max}} \ln \frac{T_{min}}{T_{max}} \right) \quad (3.9)$$

Most of the  $\delta$ -electrons have small momenta and are bent out of the acceptance. The number of electrons that reach the MVD depend on the integral of the magnetic field

$$Br = \frac{p}{q}. \quad (3.10)$$

The CBM magnet has a total bending power of  $1 Tm$ . At the location of the MVD stations the magnetic field has reached about 70 % of its maximum value [28]. This results in an approximate field integral of  $0.7 Tm$ . The minimum momentum of an electron required to reach the first MVD station  $z = 5 cm$  then is

$$T_{min} \simeq p_{min} = 300 \frac{\text{MeV}}{c} \frac{C \cdot s}{kg \cdot m} \cdot 0.7 \frac{kg}{C \cdot s} \cdot 0.05 m \simeq 10.5 \frac{\text{MeV}}{c} \quad (3.11)$$

and for the second station at  $z = 10 cm$  it is

$$T_{min} \simeq 21 \frac{\text{MeV}}{c}. \quad (3.12)$$

Equation 3.9 then gives 16  $\delta$ -electrons per incident ion at the first station and 6.5 at the second station.

Setup	Signal Efficiency	S/B
Ideal PID		
No MVD	$0.34 \pm 0.01$	$0.14 \pm 0.01$
MVD, No $\delta e^-$	$0.27 \pm 0.01$	$0.24 \pm 0.01$
MVD, 100 $\delta e^-$ events	$0.22 \pm 0.01$	$0.23 \pm 0.01$
Realistic PID		
No MVD	$0.099 \pm 0.005$	$0.060 \pm 0.003$
MVD, No $\delta e^-$	$0.066 \pm 0.004$	$0.076 \pm 0.005$
MVD, 100 $\delta e^-$ events	$0.055 \pm 0.007$	$0.073 \pm 0.009$

Table 3.10: Comparison of setups without the MVD, with the MVD but without  $\delta$ -electrons and finally with the MVD and  $\delta$ -electrons added. The simulations only had in-medium  $\rho$  embedded. Results are for the relevant mass range of  $0.55 \text{ GeV}/c^2 \leq m_{inv} \leq 1.2 \text{ GeV}/c^2$ .

Table 3.10 shows a comparison between simulations without the MVD in the geometry setup, with the MVD in the geometry setup and finally with the MVD and  $\delta$ -electron events included. While  $\delta$ -electrons have a negligible effect on the signal-to-background a substantial signal loss can be observed. The track topology cut no longer offers a good distinction between signal and background tracks (figure 3.43).

It is necessary to reduce the effects  $\delta$ -electrons have on the dielectron analysis. One possibility would be to decrease amount of  $\delta$ -electrons per readout frame by reducing the beam intensity and thus the interaction rate or by further improving the readout time of the MVD sensors. Moving the first MVD station further away from the target or removing it all together would also reduce the number of  $\delta$ -electrons that reach the first station. However, that would also decrease the benefit the MVD provides at reconstructing more low momentum tracks.

### 3.8.4 Magnetic Field Strength

It could be expected that a lower field strength would increase the amount of reconstructed low momentum tracks as they are not bent out of the acceptance of the tracking detectors by the magnetic field. Simulations with a field strength of 70% showed an increase in signal efficiency, but the additional background tracks also resulted in a lower signal to background ratio compared to the full field (tables 3.11 and 3.12). The significance is slightly higher with ideal PID, but lower with the realistic PID. There is currently no benefit running with a lower magnetic field.

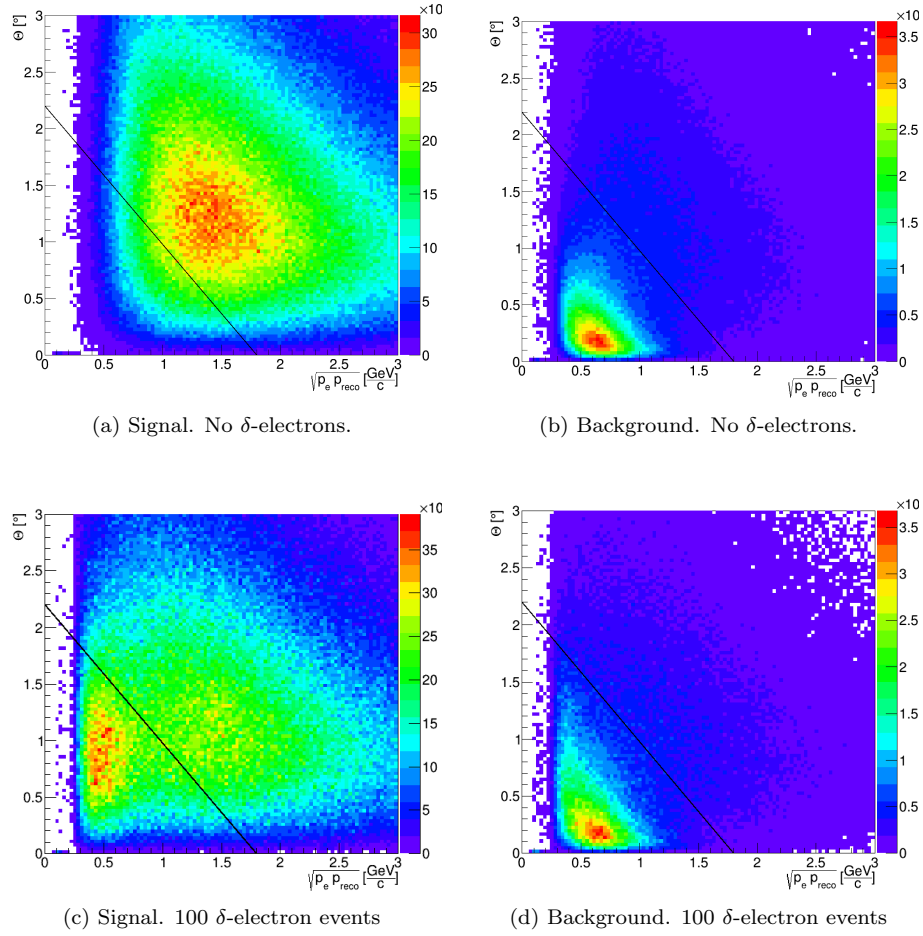


Figure 3.43: The track topology cut for signal and background sources with and without  $\delta$ -electrons. Ideal PID has been used.

Field Strength	Signal Efficiency	S/B	Significance
Ideal PID			
0.7	$0.33 \pm 0.01$	$0.19 \pm 0.01$	$13.9 \pm 0.1$
1.0	$0.27 \pm 0.01$	$0.24 \pm 0.01$	$14.2 \pm 0.1$
Realistic PID			
0.7	$0.083 \pm 0.005$	$0.054 \pm 0.003$	$3.96 \pm 0.01$
1.0	$0.047 \pm 0.004$	$0.11 \pm 0.01$	$4.16 \pm 0.01$

Table 3.11: Analysis results for different values of magnetic field strength in the invariant mass range of 0.55 GeV to 1.2 GeV. Included are only dilepton decays from the in-medium  $\rho$ .

Field Strength	Both Identified	Identified / Re-constructed	Identified / Not Reconstructed
Ideal PID			
0.7	0.37	0.57	1.76
1.0	0.19	0.42	1.26
Realistic PID			
0.7	0.091	0.46	0.65
1.0	0.056	0.31	0.55

Table 3.12: The number of dielectron decays from  $\gamma$ -conversions where particle identification for at least one lepton is available. The partner may be either identified as well, only reconstructed in the MVD and STS or not reconstructed at all.

## Chapter 4

# Summary

The performance of the dielectron analysis has been compared with and without the MVD in the geometry setup using an up to date version of the cbmroot software package. With ideal particle identification, i.e. only checking for acceptance in the PID detectors, and without  $\delta$ -electrons in the simulation the MVD helped to improve the signal-to-background ratio by around 40% while reducing the signal efficiency by around 20% in the relevant mass region between  $0.55 \text{ GeV}/c^2$  and  $1.2 \text{ GeV}/c^2$ . The significance is 10% higher. Under these ideal conditions the MVD offers a small benefit. With realistic particle identification the performance with the MVD is on the same level as without the MVD.

The additional material of the MVD results in 35% more background after particle identification. This background is produced close to the target and can not be effectively reduced by the primary vertex cut. Introducing another cut that asks for acceptance of tracks in the first MVD station helped to alleviate this issue. All other attempts to identify electrons from photon conversions failed. The impact of the additional background becomes even more severe when using realistic particle identification as it increases the probability to have partially identified pairs. With realistic PID the performance is already better without the MVD. The track topology cut becomes ineffective when adding  $\delta$ -electrons into the simulation. The performance of the dielectron analysis is better without the MVD.



# Zusammenfassung

## Einführung

Das **C**ompressed **B**aryonic **M**atter (CBM) wird an der geplanten Beschleunigeranlage FAIR (**F**acility for **A**ntiproton and **I**on **R**esearch in Darmstadt, Deutschland, betrieben werden. Das CBM Physik Programm umfasst die Untersuchung von Eigenschaften baryonischer Materie bei hohen Dichten und mittleren Temperaturen.

Quanten Chromo Dynamik (QCD) ist die Theorie der starken Wechselwirkung und beschreibt die Quarks, Gluonen und deren Wechselwirkungen. Aufgrund der Symmetrien von QCD und asymptotischen Freiheit wird bei hohen Temperaturen und Dichten ein Phasenübergang von hadronischer Materie zum Quark Gluon Plasma vorhergesagt. Mit Schwerionenkollisionen wird versucht, solche Bedingungen für kurze Zeit herzustellen. Die leichten Vektormesonen  $\rho$ ,  $\omega$  und  $\phi$  werden in der heißen, dichten Phase einer Schwerionenkollision produziert und können mit einer kleinen Wahrscheinlichkeit in Dileptonen zerfallen. Da Leptonen nicht der starken Wechselwirkung unterliegen, verlassen sie die Kollisionszone nahezu wechselwirkungsfrei. Dies macht sie zu einer guten Observablen um nach Änderungen von Hadronen im Medium zu suchen, die ein Hinweis auf die erwartete Wiederherstellung der spontan gebrochenen chiralen Symmetrie wären.

Unvollständig identifizierte Paare aus  $\pi^0$ -Dalitz Zerfällen und  $\gamma$ -Konversion tragen hauptsächlich zum Untergrund bei. In dieser Arbeit wurden Untersuchungen zum möglichen Einsatz des CBM-Micro Vertex Detectors (MVD) zur Untergrundunterdrückung in der Dielektronen Analyse durchgeführt.

## Analyse

Es wurden Simulationen zur Messung von Dielektronen mit zentralen  $^{197}\text{Au} + ^{197}\text{Au}$  Kollisionen bei der SIS-100 Energie von 8 AGeV durchgeführt. Der Impuls der Teilchen wird in den MVD und STS Detektoren rekonstruiert. Für die Teilchenidentifikation werden der RICH Detektor sowie, sofern verfügbar, Informationen vom TRD und TOF verwendet.

Das CBM-Detektorkonzept unterscheidet sich von anderen Dielektronen-Experimenten wie HADES oder CERES dadurch, dass die Detektoren zur Teil-

chenidentifikation sich hinter dem Magnetfeld und den Detektoren zur Impulsrekonstruktion befinden. Dies hat zur Folge, dass Elektronen aus  $\gamma$ -Konversionen den RICH erreichen können und zum Untergrund beitragen. Ausserdem lassen sich Paare aus Untergrundquellen nicht mehr anhand ihres charakteristisch geringen Öffnungswinkels identifizieren.

Um auszuschliessen, dass die PID Detektoren das Ergebnis beeinflussen, wurde zunächst eine ideale Elektronenidentifikation verwendet, bei der nur die Akzeptanz im RICH, TRD und TOF verlangt wurde.

Für eine realistischere Teilchenidentifikation wurden die rekonstruierten Informationen vom RICH, TRD und TOF verwendet: die Antworten der neuronalen Netze vom RICH und TRD sowie die relativistische Geschwindigkeit  $\beta$  in Abhängigkeit vom Impuls für den TOF. Um die Schnitte zur Elektronenidentifikation zu bestimmen wurden verschiedene Kriterien angewandt und verglichen. Zum einen wurden die Schnitte so gewählt, dass die Signifikanz maximal ist, die Genauigkeit am größten, die Effizienz zur Elektronenerkennung 90% und 80% beträgt. Die Signifikanz ist definiert als

$$\text{Signifikanz} = \frac{\text{Signal}}{\sqrt{\text{Signal} + \text{Untergrund}}}.$$

Die Genauigkeit ist

$$\begin{aligned} \text{Genauigkeit} &= \frac{1}{2} (\text{Sensitivität} + \text{Spezifizität}) \\ \text{Sensitivität} &= \frac{\text{Anzahl korrekt identifizierter Elektronen}}{\text{Anzahl Elektronen}} \\ \text{Spezifizität} &= \frac{\text{Anzahl Untergrund als Elektronen identifiziert}}{\text{Anzahl Untergrund}}. \end{aligned}$$

Zusätzlich wurden die Schnitte mit dem Tool for MultiVariate Analysis (TMVA) optimiert. Zum Untergrund tragen hauptsächlich falsch identifizierte Pionen und Protonen bei sowie falsch zugeordnete Spuren aus dem STS Detektor. Die Schnitte, die die einzelnen Signifikanzen maximieren, haben sich als die effektivsten herausgestellt.

In einem letzten Schritt wurden  $\delta$ -Elektronen in die Simulation eingebunden. Die Analyse wurde immer mit und ohne dem MVD im Detekoraufbau wiederholt.

Die Strategie zur Untergrundunterdrückung beinhaltet folgende Schritte: Spuren werden zum rekonstruierten primären Vertex extrapoliert und anhand der Extrapolationsgüte verworfen. Zusätzlich wird gefordert, dass Spuren in der Akzeptanz der ersten MVD Detektorstation liegen. Durch diese Schnitte sollen Teilchen aus  $\gamma$ -Konversionen, die ausserhalb der Targetregion produziert werden, zu identifizieren. Dieser Schritt ist weniger effektiv bei  $\gamma$ -Konversionen, die in den MVD Stationen erzeugt werden als bei solchen, die im STS entstehen. Um die Effektivität dieses Schnittes zu verbessern, wird ausserdem verlangt, dass einer rekonstruierten Spur entweder ein Hit in der ersten MVD Station zugewiesen ist. Ist dies nicht der Fall, wird die Spur zur ersten

MVD Station extrapoliert und aus der Analyse entfernt, falls die extrapolierten Ortskoordinaten außerhalb der äußeren Akzeptanz der MVD Station liegen. Da ein beträchtlicher Teil der Teilchen aus dem primären Vertex das innere Strahlloch des MVD passiert, werden nur Spuren nicht akzeptiert, die in der äußeren Akzeptanz liegen.

Um teilweise identifizierte Untergrundpaare zu erkennen, wird ein Topologie angewandt, basierend auf dem Öffnungswinkel und Produkt der Impulse von nahe beieinander liegenden Spuren. Paare aus Photonkonversionen und  $\pi^0$ -Dalitz Zerfällen zeichnen sich durch kleine Öffnungswinkel und niedrige Impulse aus. Dieser Schnitt zeigt ohne die Einbindung von  $\delta$ -Elektronen eine bessere Trennung von Signal und Untergrund durch den MVD.

Weitere Schnitte zur Reduzierung des Untergrunds wurden untersucht. Die gute Positionsauflösung bot die Aussicht, Elektronenpaare mit kleinen Öffnungswinkeln zu identifizieren. Die Anwendung eines Schnittes basierend auf dem Abstand der Hits eines identifizierten Elektrons und seinem nächsten Nachbarn erwies sich als ineffektiv, da das Magnetfeld vor der ersten MVD Station bereits so hoch ist, dass Paare aus Photonkonversionen zu weit geöffnet sind, wenn sie diese erreichen.

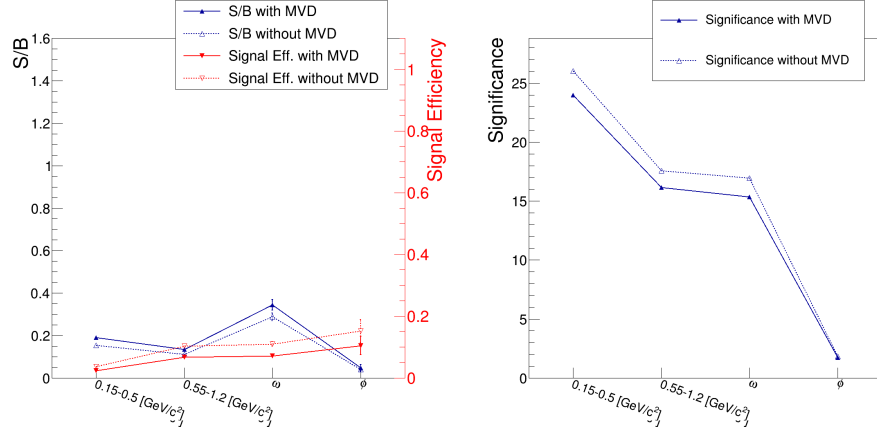
Ein anderer Ansatz war Paare aus Photonkonversionen im MVD zu finden, wo ein Teilchen identifiziert wurde und der Partner nicht rekonstruiert werden konnte, aber genügend Hits im MVD hinterlassen hat um rekonstruierbar zu sein. Die rekonstruierte Spur aus einer Photonkonversion wurde zum Monte Carlo Zerfallsvertex extrapoliert. Die anfängliche Position und Richtung des Partners folgen aus der Extrapolation und der Impuls ergibt sich daraus, dass  $\gamma$ -Konversionen einen kleinen Öffnungswinkel und niedrige invariante Masse haben. Eine Spur mit den entsprechenden Startwerten wird durch den MVD propagiert und innerhalb eines Suchfensters Hits zugewiesen. Selbst unter diesen ideal Bedingungen wurden nur 25% aller Spurkandidaten gefunden. Während nach der Extrapolation gute Startwerte für Position und Richtung vorliegen, ist die Unsicherheit beim Impuls zu gross, so dass dieser Ansatz nicht praktikabel ist.

KFParticle ist ein Paket zur Bestimmung sekundärer Vertices und Berechnung der Parameter der Zerfallsteilchen. Der *KFParticleFinder* beinhaltet die Rekonstruktion von Paaren aus  $\gamma$ -Konversionen. Es werden nur etwa 1.5% aller Photonkonversionen außerhalb der Targetregion gefunden, da die Wahrscheinlichkeit, dass beide Teilchen eines Paares erfolgreich durch die PID identifiziert werden, gering ist.

Mit idealer PID und ohne  $\delta$ -Elektronen überwiegen noch die Vorteile, die der MVD beim Topologieschnitt bringt. Es ergibt sich eine kleine Steigerung der Signifikanz um 10%, wenn der MVD in der Analyse verwendet wird. Bei realistischer PID ist die Signifikanz ohne den MVD leicht besser (Abb. 4.1).

Werden schliesslich noch  $\delta$ -Elektronen eingebunden, ist auch beim Topologieschnitt eine Trennung von Signal und Untergrund mit dem MVD nicht mehr möglich.

Der MVD produziert zusätzlichen Untergrund, der nicht mehr effektiv durch die Extrapolation zum primären Vertex identifiziert werden kann. Die  $\delta$ -Elek-



(a) Signal zu Untergrund sowie Signaleffizienz mit und ohne dem MVD.

(b) Signifikanz mit und ohne dem MVD.

Figure 4.1: Vergleich von Signal zu Untergrund, Signaleffizienz und Signifikanz mit und ohne dem MVD im Geometriesetup für realistische Teilchenidentifikation.

tronen führen dazu, dass die Effektivität des Topologieschnittes reduziert ist. Dies macht eine Verwendung des MVD in der Dielektronenanalyse nicht sinnvoll.

# Bibliography

- [1] D. Adamova and others (CERES Collaboration). Enhanced production of low mass electron pairs in 40a gev pb-au collisions at the cern sps. *Phys. Rev. Lett.*, 91(042301), 2003. 14
- [2] D. Adamova and others (CERES Collaboration). Modification of the rho meson detected by low-mass electron-positron pairs in central pb+au collisions at 158 agev. *Phys. Lett.*, B666:425, 2006. 13
- [3] G. Agakishiev and others (CERES Collaboration). Low mass e+e- pair production in 158 a-gev pb-au collisions at the cern sps, its dependence on multiplicity and transverse momentum. *Phys. Lett.*, B422:405–412, 1998. 3, 13, 14
- [4] G. Agakishiev and others (HADES Collaboration). Dielectron production in c-12+c-12 collisions at 2-agev with hades. *Phys. Rev. Lett.*, 98(052302), 2007. 14
- [5] G. Agakishiev and others (HADES Collaboration). Study of dielectron production in c+c collisions at 1-a-gev. *Phys. Lett.*, B663:43–48, 2008. 14
- [6] G. Agakishiev and others (HADES Collaboration). Origin of the low-mass electron pair excess in light nucleus-nucleus collisions. *Phys. Lett.*, B690:118–122, 2010. 14
- [7] G. Agakishiev and others (HADES Collaboration). Dielectron production in ar+kcl collisions at 1.76a gev. *Phys. Rev.*, C84(014902), 2011. 3, 14, 15
- [8] R. Arnaldi and others (NA60 Collaboration). Evidence for the production of thermal-like muon pairs with masses above 1 gev/c in 158a gev indium-indium collisions. *Eur. Phys. J.*, C59:607–623, 2009. 14
- [9] R. Arnaldi and others (NA60 Collaboration). Na60 results on thermal dimuons. *Eur. Phys. J.*, C61:711–720, 2009. 14
- [10] J. Book. Private communication. 7, 24
- [11] Peter Braun-Munzinger, Volker Koch, Thomas Schäfer, and Johanna Stachel. Properties of hot and dense matter from relativistic heavy ion collisions. arXiv:1510.00442 [nucl-th], 2015. 3, 12, 16

- [12] Gerald E. Brown and Mannque Rho. Scaling effective lagrangians in a dense medium. *Phys. Rev. Lett.*, 66(21):2720, 1991. 13
- [13] S. Chattopadhyay. Technical design report for the cbm muon chamber system. Technical Report (GSI-2015-02580), GSI Darmstadt, 2015. 21
- [14] M. Dey, V.L. Eletsky, and B.L. Ioffe. *Phys. Lett.*, B252:620, 1990. 13
- [15] K. Dusling and I. Zahed. Transverse momentum spectra of dileptons measured by the na60 collaboration in inin collisions at 158 gev/nucleon. *Phys. Rev.*, C80(014902), 2009. 3, 14, 15
- [16] C. Höhne (editor). Technical design report for the cbm ring imaging cherenkov detector. Technical Report (GSI-2014-00528), GSI Darmstadt, 2013. 20, 21, 27
- [17] N. Herrmann (editor). Technical design report for the cbm time-of-flight system (tof). Technical Report (GSI-2015-01999), GSI Darmstadt, 2014. 21
- [18] B. Friman, C. Höhne, J. Knoll, S. Leupold, J. Randrup, R. Rapp, and P. Senger (editors). *The CBM Physics Book*. Lecture Notes in Physics, Vol. 814 1st Edition. Springer, 2011. ISBN-978-3-642-13292-6. 1, 10, 17
- [19] I. Froehlich et al. Pluto: A monte carlo simulation tool for hadronic physics. *PoS ACAT2007:076*, 2007. 23
- [20] T. Galatyuk. Di-electron spectroscopy in hades and cbm: from p+p and n+p collisions at gsi to au+au collisions at fair. Master’s thesis, Goethe-Universität Frankfurt am Main, 2009. 47
- [21] S. Gorbunov and I. Kisel. An analytic formula for track extrapolation in an inhomogeneous magnetic field. CBM-SOFT-note-2005-001. 26
- [22] F. Guber and I. Selyuzhenkov (editors). Technical design report for the cbm projectile spectator detector (psd). Technical Report (GSI-2015-02020), GSI Darmstadt, 2015. 22
- [23] J.M. Heuser et al. Technical design report for the cbm silicon tracking system (sts). Technical Report (GSI-2013-05499), GSI Darmstadt, 2013. 19, 21, 26
- [24] A. Hoecker et al. *TMVA - Toolkit for Multivariate Data Analysis with ROOT*, October 2013. [tmva.sourceforge.net/docu/TMVAUsersGuide.pdf](https://tmva.sourceforge.net/docu/TMVAUsersGuide.pdf). 30
- [25] I. Kisel. Event reconstruction in the cbm experiment. *Nucl. Instr. Meth. Phys. Res.*, A566:85, 2006. 26

- [26] I. Kisel. Reconstruction of tracks in high energy physics experiments. Habilitationsschrift zur erlangung der venia legendi für das fach physik, Ruprecht-Karls-Universität Heidelberg, 2008. 26
- [27] A. Lebedev et al. Track reconstruction algorithms for the cbm experiment at fair. *J. Phys Conf. Series*, 032048:219, 2010. 27
- [28] A. Malakhov and A. Shabunov (editors). Technical design report for the cbm superconducting dipole magnet. Technical Report (GSI-2015-02000), GSI Darmstadt, 2013. 3, 19, 20, 65
- [29] K.A. Olive and others (Particle Data Group). Review of particle physics. *Chinese Physics C*, 38(090001), 2014. 7, 13, 24
- [30] W. Peters, M. Post, H. Lenske, S. Leupold, and U. Mosel. The spectral function of the rho meson in nuclear matter. *Nucl. Phys.*, A632, 109-127. 13
- [31] R. Rapp and J. Wambach. Chiral symmetry restoration and dileptons in relativistic heavy ion collisions. *Adv. Nucl. Phys.*, G35, 2000. 14, 23
- [32] J. Rupert, C. Gale, T. Renk, P. Lichard, and J.I. Kapusta. Low mass dimuons produced in relativistic nuclear collisions. *Phys. Rev. Lett.*, 162301:100, 2008. 3, 14, 15
- [33] F. Seck. Private communication. 7, 24
- [34] F. Seck et al. Towards a realistic event generator for in-medium and qgp dileptons. *CBM Progress Report*, 2014. 23
- [35] Hans J. Specht. Thermal dileptons from hot and dense strongly interacting matter. *AIP Conf. Proc.*, 1322:1–10, 2010. 3, 14, 15
- [36] T. Tischler. Mechanical integration of the micro vertex detector for the cbm experiment. Master’s thesis, Goethe-Universität Frankfurt, 2015. 19
- [37] C. Trageser. Systematische untersuchung zur auswirkung der detektor-geometrie auf die spurrekonstruktionseffizienz und stoßparameterauflösung des cbm mikro-vertex-detektor. Master’s thesis, Goethe-Universität Frankfurt, 2012. 19
- [38] H. van Hees and R. Rapp. Dilepton radiation at the cern super proton synchrotron. *Nucl. Phys.*, A806:339–387, 2008. 3, 14, 15
- [39] Nu Xu. An overview of star experimental results. *Nucl. Phys.*, A931, 2014. 14
- [40] W-M Yao et al. Nuclear and particle physics. *J. Physics*, G 33:299, 2006. 7, 13

# Curriculum Vitae

<b>Personal Data:</b>	Name:	Erik Krebs
	Address:	In den Birkenäckern 30 64291 Darmstadt
	Date of birth:	21/09/1973
	Nationality:	German
	Place of birth:	Königstein im Taunus, Germany
<b>Higher education:</b>	Since 10/11	PhD student at Goethe University, Frankfurt am Main
	10/06 – 09/11	Master of Science Goethe University, Frankfurt am Main Major: Physics Minors: Astrophysics, Numerical Mathematics Thesis Title: „Application of a Kalman filter and a Deterministic Annealing filter for track reconstruction in the HADES experiment“
	10/95 – 03/04	Diploma University Stuttgart Major: Computer Science Minor: Chemistry Thesis Title: „Paritätsspiele“
	10/93 – 09/95	Aerospace technology at the University Stuttgart No degree
	05/93	Abitur (eq. to GCE Advanced Level) Kurpfalz-Gymnasium Mannheim Majors: Mathematics, Physics
<b>Secondary education:</b>		

Darmstadt, 17/08/16



## ERKLÄRUNG

Ich erkläre hiermit, dass ich mich bisher keiner Doktorprüfung im Mathematisch-Naturwissenschaftlichen Bereich unterzogen habe.

Frankfurt am Main, den .....

Unterschrift

## Versicherung

Ich erkläre hiermit, dass ich die vorgelegte Dissertation über

.....

.....

.....

selbständig angefertigt und mich anderer Hilfsmittel als der in ihr angegebenen nicht bedient habe, insbesondere, dass alle Entlehnungen aus anderen Schriften mit Angabe der betreffenden Schrift gekennzeichnet sind.

Ich versichere, die Grundsätze der guten wissenschaftlichen Praxis beachtet, und nicht die Hilfe einer kommerziellen Promotionsvermittlung in Anspruch genommen zu haben.

Frankfurt am Main, den .....

(Unterschrift)